An oceanographic pressure sensor based on an in-fibre Bragg grating

by

Riccardo Alessandro Bostock
BASc, Queens University, 2017

A Thesis Submitted in Partial Fulfillment
of the Requirements for the Degree of

MASTER OF APPLIED SCIENCE

in the Department of Mechanical Engineering

Supervisory Committee

An oceanographic pressure sensor based on an in-fibre Bragg grating
by

Riccardo Alessandro Bostock
BASc, Queens's University, 2017

Supervisory Committee

Dr. Peter Wild, Department of Mechanical Engineering
Supervisor

Dr. Mohsen Akbari, Department of Mechanical Engineering
Departmental Member

Abstract

Supervisory Committee
Dr. Peter Wild, Department of Mechanical Engineering
Supervisor

Dr. Mohsen Akbari, Department of Mechanical Engineering
Department Member

Deep-ocean pressure measurements are a necessary component for ocean characterization and oceanographic monitoring. Some principle applications such as tsunami detection and ocean floor subsidence are reliant on deep-ocean pressure measurement data. The deep ocean is a challenging environment especially for pressure measurements; discerning pressure changes that are a small fraction of the ambient pressure calls for intelligent engineering solutions.

An ocean-deployable concept model of a pressure sensor is developed. The design is based on a diaphragm transducer intended for measuring hydrostatic pressure changes on the order of 1 centimeter of water (cmH$_2$O) while exposed to ambient pressures several orders of magnitude greater for up to 2500 meters of water (mH$_2$O). Two laboratory-scale pressure sensors are fabricated to test the fundamental principle of the proposed concept at lab-safe pressures. One is a single-sided sensor exposed to atmospheric pressure. The second sensor is a two-sided design that operates at a defined target depth pressure and measures the differential pressure across both faces of the diaphragm.

The sensor design built for atmospheric pressure testing observed a mean experimental sensitivity of 6.05 pm/cmH2O in contrast to 6 pm/cmH$_2$O determined theoretically. The percent error between the experimental and theoretical values is 0.83%. The second design was tested at target depth pressures of 10, 20, 40, and 60 psi (7, 14, 28, and 42 mH2O) and performance was within 5.8%, 2.8%, 0.7%, 4.0% respectively when considering percent error of the mean experimental and theoretical. The repeatability was sufficient for a given sample and pressure response within the range proposed in theory when a pressure preload was present to the diaphragm. Future work will aim at developing a design concept that incorporates a piston and is tested at a higher hydrostatic pressure system, and within ocean waters. A deployment plan and consideration of challenges associated with ocean testing will be accounted for.

Table of Contents

List of Tables

List of Figures

Acknowledgments

First and foremost, my gratitude towards Dr. Peter Wild for his ongoing support throughout my tenure cannot be expressed enough. His guidance, knowledge, and supportive attitude facilitated and made this work possible. I would like to thank Rodney Katz for his assistance in fabrication of all the inhouse sensor components and the sharing of his machining insight that I will serve in my future engineering endeavours. I must also thank Reza Harirforoush and Mattias Aigner both for their assistance in my experimental trials and FEA assistance in addition to their enriching presence in the Optical Sensors Laboratory.

To Pauline Shepherd and Susan Walton of the IESVIC office, you were truly the best one could ask for. Your warm natures always created such a welcoming environment in the office and made coming in every day very pleasant. Lastly, to all of those that I shared lunch time talks and engaging conversations with throughout the office: Mattias, Reza, Sven, Cameron, Kevin, Jennifer, Adriano, Sean, McKenzie, and Victor, I thank you all.

Dedication

This work is dedicated to my family, Chiara, Eliana, and Michael. This is also dedicated to my family in Italy and Toronto, and to my late Nonna, who passed away during the finishing stages of this work.

Chapter 1 - Introduction

1.0 Introduction

In this thesis, the focus is to design and test a pressure sensor intended for taking measurements at the ocean-bottom to quantify small pressure perturbations in large ambient pressure ranges. This is a situation that arises in oceanographic circumstance such as seafloor vertical deformation or tsunami detection and characterization.

1.1 Ocean-bottom pressure measurements

The use of ocean-bottom pressure sensors in monitoring vertical deformation in the seafloor is important for providing information on changes in the Earth's crust including earthquakes, tsunamis, and slow slip events [1]. To gather useful seafloor deformation data, an ocean-bottom pressure sensor should resolve pressure changes to within the centimeters of water [2]. For example, monitoring vertical deformation at Axial Seamount after 1998 eruption was done so in the range of tens of centimeters at a depth of 1500 m [3].

The necessity for detection of a tsunami in particular, is important to inhabitants of coastal regions to enable early warnings that can reduce causalities when a tsunami occurs. Large tsunami events such as the 2004 Indian Ocean and 2011 Tōhoku tsunamis are some of the most extreme examples in recent times. These events and the possibility of future tsunami occurrences stress the necessity to develop improved advanced warning systems.

A tsunami is a series of waves that propagate through the ocean, containing energy capable of displacing a volume of water larger than typical ocean waves. The cause of a tsunami can vary from earthquake, submarine landslide, volcanic eruption, meteorite impact, or other high energy triggers. The most common causes of tsunamis are earthquakes, specifically in subduction zones in the ocean [4].

As a tsunami travels across the open ocean, it can reach speeds of up to 950 km/h and is capable of crossing an entire ocean [4]. In the deep-ocean, tsunami wavelengths can reach up to two hundred kilometers, while ranging from a few centimeters to one metre in height [5]. Tsunamis of different magnitudes and sources share a similar behaviour as they pass through various depths of water to arrive ashore. The magnitude and type of tsunami triggering event will determine the wavelength and period of the waves, but as these long-period waves radiate away from the source and reach shallower water, the wavelength and wave speed energy is converted into vertical energy which causes the amplitude to grow. This phenomenon is described by Green's Law [6], shown in Equation (1.1).

$$(H_1)^4 h_1 = (H_2)^4 h_2 \tag{1.1}$$

Here, H_1 and H_2 represent the height of a passing wave at two different locations, and h_1 and h_2 are the mean water depths at the respective locations. This relation approximates the height change that occurs as a tsunami changes location, such as when a wave in the open ocean moves into shallow waters.

Loss of energy as a tsunami travels in deep-waters are minimal and result mainly from friction losses due to water viscosity. As a tsunami approaches the continental shelf, energy losses are associated primarily with friction with the ocean floor and conversion of kinetic energy to potential energy as the wave rises in amplitude and decreases in wavelength and speed [7].

As mentioned, tsunami amplitudes in the open ocean typically are within several centimetres to a meter, therefore the associated pressure perturbation can be 6 or 7 orders of magnitude smaller than ambient hydrostatic pressure applied at the seafloor; where bottom pressure sensor would be deployed [8]. For example, a sensor built to operate at up to 2000 m of depth would require a resolution of 0.0005% FS to detect 1 cmH_2O.

The purpose of this study is to design a pressure sensor with a resolution of 1 cmH_2O, which can operate in depths of up to 2500m, which is considered in the deep ocean depth range [9]. This depth is selected with reference to [2] and is in accordance with the pressure limits that allow the Ideal Gas law to be applicable for modeling (this is examined in further detail in subsequent sections). The seafloor crustal deformation in Hikurangi Margin, New Zealand was monitored with sensors deployed at depths varying from 651m to 3532m so a depth of 2500 m falls between these values [2].

The target resolution was determined based on [10], which outlines the Deep-ocean Assessment and Reporting of Tsunamis (DART) used in the Ring of Fire and parts of the Indian Ocean. In 2003 when a 7.5 magnitude earthquake off the coast of Alaska produced a tsunami amplitude of 2 cm in deep-ocean caused which caused tsunamis that was detected by the DART system. Thus, the designation of centimeter-based resolution is adequate for tsunami detecting instruments.

1.2 Commercial Deep-Ocean Pressure Sensors

Four commercially available deep ocean bottom pressure sensors have been identified: Sea-Bird SBE 50, Valeport miniIPS, GE PRECISE DPS2000 Series, and the Digiquartz Depth Sensor Series 8000. The specifications of these sensors are presented in Table 1.

Table 1: Specifications of commercially available pressure sensors. Pressure specifications have been converted to mH_2O to allow comparison.

	Sea-Bird SBE 50 [11]	**Valeport miniIPS [12]**	**GE DPS2000 [13]**	**Digiquartz Depth Sensor Series 8000 [14]**
Selected Range (mH_2O)	600	1020	3060	2000
Accuracy (cmH_2O)	±60	±10	±30	±20
Resolution (mmH_2O)	12	10	6	1
Sampling Rate	16 Hz	8 Hz	Not Specified	180 Hz
Weight (kg)	0.7	1	-	1.5-3.6
Length (mm)	265	185	165	55
Diameter (mm)	390	400	230	268
Price (USD)	\$3,400	\$4,525	\$5,575	\$10,475

Various models are available from each supplier. The sensor models in presented in Table 1 are those with ranges that are closest to the target resolution of 1 cmH_2O.

The Sea-Bird Scientific SBE 50 Digital Oceanographic Pressure Sensor, uses strain-gauge elements bonded to a diaphragm and is temperature compensated. This unit is available for eight pressure ranges between 0-20 to 0-7000 mH_2O with a resolution and accuracy of 0.002% and ±0.1% of full-scale respectively. The sensor cost is \$3,400 USD which is the most inexpensive of these four sensors [11]. The model considered for the comparison is rated for 600 m and with a resolution of 12 mm. This resolution nearly matches the target resolution proposed for the design in this thesis however the respective operating range is nearly 4 times less than the target.

The Valeport miniIPS is a piezoresistive sensor with a stainless-steel diaphragm and temperature compensation. Piezoresistors are sensitive to properties that induce strain and function by changing resistance when the material deforms. These materials are highly sensitive but have nonlinear resistance-input profiles and require a reference voltage [15]. With that said, the available models cost \$4,525 USD and are rated for up to 6100 mH_2O

with a resolution and accuracy of 0.001% and ±0.01% of full-scale, respectively. The miniIPS model examined for this comparison is rated for 1020 mH_2O with a resolution of 1 cmH_2O which is better than the SBE 50 but does not meet the operating pressure target of the current study.

The General Electric (GE) PRECISE DPS2000 Series digital pressure transmitter is another oceanographic sensor for deep water measurements and tsunami detection. This piezoresistive sensor contains a single silicon crystal structure with a tubular design that allows measurement within a resolution of 0.0002% FS over a pressure range of up to 15,092 mH_2O. This sensor has the greatest maximum rated depth of other compared sensors, going beyond depths of the Mariana's Trench [13]. Considering the example model selected for comparison, the rated depth is 3060 mH_2O with a resolution of 6 mmH_2O. This sensor is available for $5,575 USD, amounting to over $1000 more than the other highlighted models.

The Digiquartz Depth Sensor Series 8000 from Paroscientific uses quartz crystal resonators to generate a signal with frequency proportional to a given input pressure. The comparison model examined in Table 1 was rated for 2000 mH_2O and able to resolve down to 1 mmH_2O.

The operating mechanism of the Paroscientific pressure transducer pressure is shown in Figure 1.

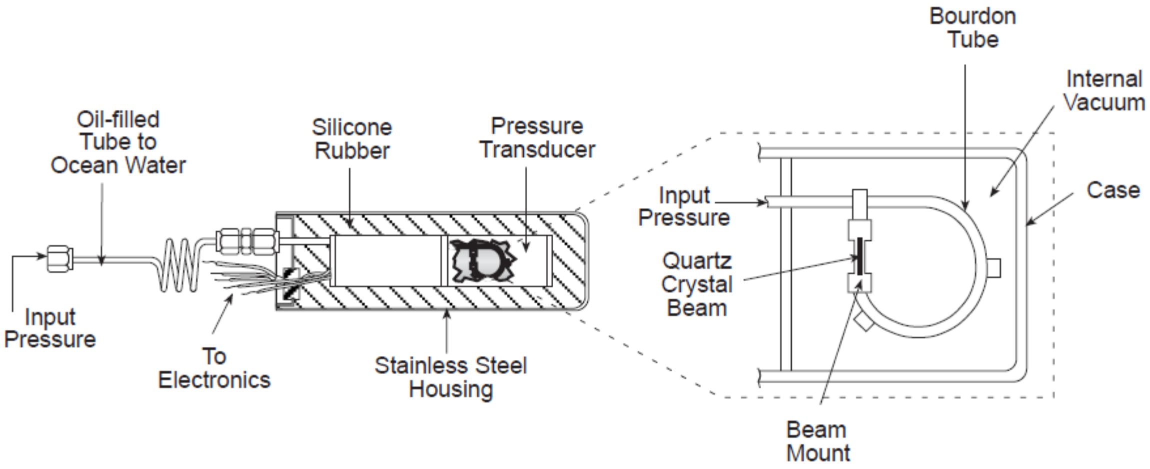

Figure 1: Paroscientfic transducer design [16]. Image reprinted with permission from American Meterological Society.

The quartz crystal beam is fixed to a Bourdon tube that is subject to a pressure input from an opening exposed to the ocean. As a pressure increase occurs, the Bourdon tube will tend to uncurl, subjecting the beam to axial strain and thereby increasing the detectable vibrating frequency of the quartz crystal. The opposite effect occurs when a pressure decrease occurs. An oscillator circuit detects vibrations on the order of 40,000 Hz while a quartz-crystal clock averages the period of all measurements. This transducer technology makes the sensor sensitive to wave height changes that are less than a millimeter. This aspect of the Digiquartz Series 8000 makes it the best option in terms of resolution than the other sensors compared, but also the costliest at $10,475 USD.

All of these pressure sensors have a comparable resolution specification, as shown in Table 1. Ultimately, resolution is the critical aspect to be considered for a pressure sensor to make small pressure measurements to detect tsunami waves. Not all sensors review, such as the SBE50 and miniIPS, are able to achieve the same operating pressure to resolution ratio as the target set.

The sensors presented in Table 1 are available at costs ranging from $3400 to $10,475 USD. An effective tsunami or deformation system requires an array of multiple sensors and the costs can exceed the available resources especially in less affluent regions of the world [17]. The following chapters will consider a design that could be produced at lower costs than these commercial options while offering similar specifications.

1.3 FBG/Diaphragm-based pressure sensors

An in-fibre Bragg grating (FBG), is a common fibre optic device, originally developed for communications applications, which has been adapted to a range of sensing applications. Unlike electrical sensing elements, FBGs are suitable for environments characterised by exposure to water and electromagnetic interference [18]. FBGs also provide the capability of multiplexing, thereby, allowing multiple sensors to be connected in series along a single fibre optic.

A number of FBG-based pressure sensor designs are reported in the literature [19] [20] [21] [22] [23].These designs include longitudinally surface bonded FBGs, an FBG in tension, and a cantilever-diaphragm FBG configuration. The type of configuration that will be focused on in this thesis is longitudinally surface bonded FBGs. This method of fixing the FBG was selected since prior work indicated had indicated this as a successfully strategy and it is simplest to execute given the assembly setting. Three of the five literary works review have deployed this fixing method, while one work has anchored perpendicularly to a diaphragm and another has an FBG bonded to a cantilever.

Huang et al. have proposed a diaphragm-FBG sensor operating that features two FBG bonded across the face of a diaphragm that is welded at the periphery as a fixture method.

The implementation of a dual FBG configuration allows one of the FBGs to be placed at the centre of the diaphragm to detect positive centre strain while the second FBG is positioned adjacent to the centre FBG along the same continuous fibre to measure negative radial strain. This is seen in Figure 2.

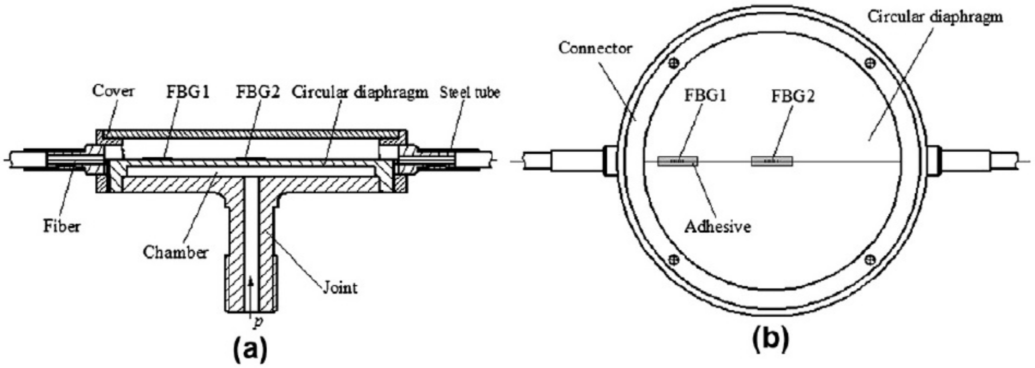

Figure 2: Diaphragm Pressure Sensor Proposed by Huang et al. [19]. Image reprinted with permission from Elsevier.

By acquiring these values of strain and knowing the positioning of the respective FBGs, the strain-temperature cross-sensitivity can be negated arithmetically. Both of the FBGs are exposed to the same temperature field, so the change in temperature is cancelled out when the Bragg wavelength expressions for each respective FBG are subtracted. This form of temperature compensation relies on the difference of shift in Bragg wavelength. This feature is advantageous as it is easily adoptable for temperature compensation. Another considerable advantage is that the diaphragm is welded to form a structure that best embodies the theoretical fixture representation as opposed to some clamping approaches. Based on the experimental results, Huang et al. have developed a design which functions linearly within 99.996% obtaining sensitivity of 1.57 pm/kPa while operating in a range of 0 to 1 MPa as seen in Table 2.

A similar approach for the design of an FBG-Diaphragm pressure sensor was developed by Allwood et al. with the use of a rubber diaphragm and single bonded FBG. The analysis developed is similar in nature with the exception of temperature compensation. Allwood et al. acknowledged that using a rubber diaphragm with such a low Young's Modulus (E= 1.4 MPa) would be subject to a reinforcing effect from the bonded FBG (E=67 GPa) and account for this in the model. The experimental sensitivity was determined to be 0.116 nm/kPa over a range of 15 kPa. An advantage to this design is the use of a rubber diaphragm which offers significantly enhanced sensitivity in comparison to many other metal-based diaphragms sensors.

While still within the pressure measurement domain, the other examined designs outlined in Table 2 are intended for liquid level monitoring applications. Two designs developed by Díaz et al. and Marques et al. measure pressure in terms of an amount of vertical water displacement. The design by Díaz et al. operates between 50 to 500 mm of vertical water displacement with a sensitivity of 2.8 pm/mmH_2O while Marques et al. achieve 57.3 pm/cmH_2O with a functional range of 0 to 75 cm. A retainer ring is deployed as a fixing and sealing apparatus in both designs. Figure 3 demonstrates the structure of the sensor proposed by Diaz et al.

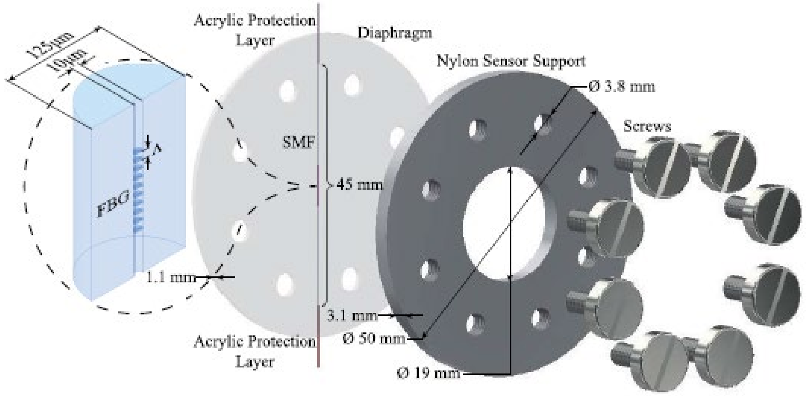

Figure 3: Sensor design proposed by Diaz et al. Image reprinted with permission from IEEE.

The advantage to applying a retainer ring as opposed to welding is ability to assemble and disassemble the device without the need for complex tools.

There are other methods of designing diaphragm-FBG sensors with novel forms of bonding and secondary functioning components to provide sensing. An FBG hydrophone concept developed by Zhang et al. is proposed as an acoustic detection device with potential use in future operational sonar systems. The design consists of a cylindrical enclosure that houses two identical piston-like diaphragms with a portion of fibre anchored normal to the centre of the face of each diaphragm. The FBG is located in between the two rubber diaphragms and is therefore sensitive to any axial displacement occurring due to centre deflection of the two diaphragms. The design incorporates the diaphragms as interfaces between airtight cavities and an opening that allows a pressure input to cause deflection in the diaphragms. A labeled diagram is seen in Figure 4 providing context on the layout of the design [24].

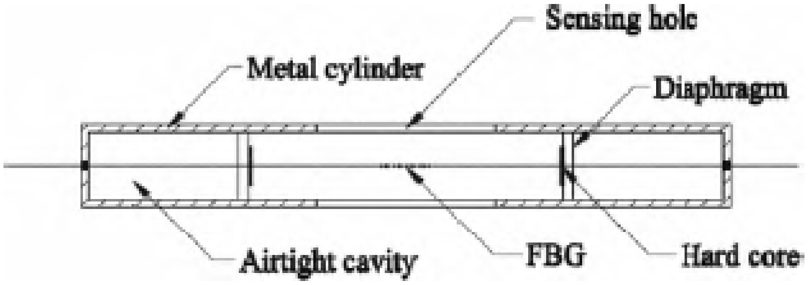

Figure 4: FBG hydrophone design by Zhang et al. [24]. Image reprinted with permission from IEEE.

There are advantages to this concept, namely in the simplicity and the symmetry of the design. With the use of a rubber diaphragm, the Young's Modulus is several orders of magnitude less stiff than metallic materials which allows for heightened sensitivity without compromising a practical geometry. With this design and diaphragm characteristic, the sensitivity achieved is 7nm/MPa operating from 0.1 to 0.2 MPa.

The concept of anchoring an FBG normal to the centre of the face of a diaphragm is a configuration that is adopted in similar work found in the pressure sensing domain of academic literature. This is seen in work done by Guo et al. and Pachava et al.

An alternative design concept is explored by Liang, et al. which incorporates a diaphragm-cantilever-FBG union to form temperature-compensated pressure sensor for megapascal sensing application. In this configuration, the diaphragm is not the direct mechanical amplifying component for the FBG but rather the cantilever. A dowel bar acts as an intermediate displacement transferring component that is attached to the free end of the cantilever and the centre of fixed diaphragm. As the diaphragm is exposed to a pressure load, the resulting deflection is transferred through the perpendicular dowel bar to the cantilever which will cause bending to occur. The strain caused by this bending in the cantilever is transmitted to the two longitudinally bonded FBGs. One of the FBGs is bonded to the cantilever face experiences tensile stress while the second FBG is bonded on the opposite face undergoes compressive stress. This feature is seen in Figure 5.

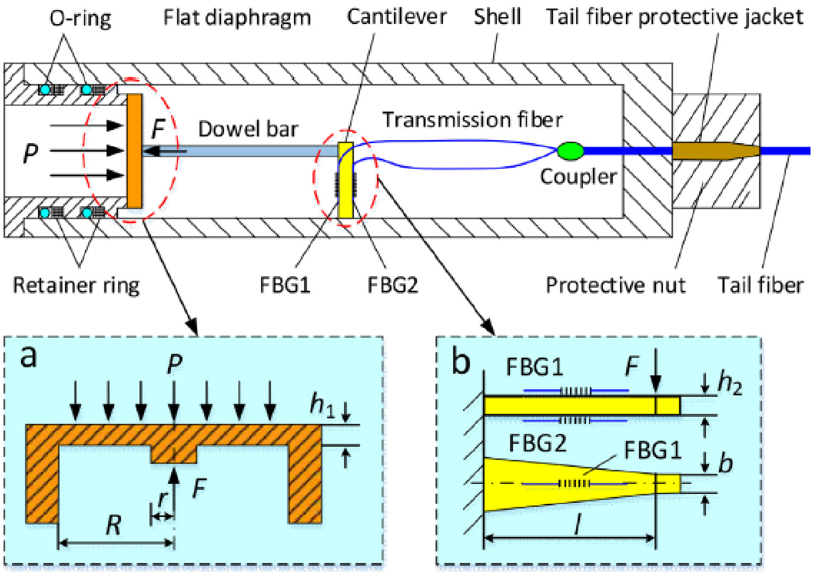

Figure 5: Cantilever-Diaphragm pressure sensor design developed by Liang, et al.

By utilizing a cantilever beam with two FBGs, the pressure-temperature cross-sensitivity effect is negated. The absolute value of measured strain is equal with the FBG in compression having negative strain while the FBG in tension has positive strain. Both of the FBGs are exposed to the same temperature field, so arithmetically the change in temperature is cancelled out when the Bragg wavelength expressions for each FBG are subtracted. Based on the experimental results, Liang et al. have developed a design which functions linearly within 99.997% and has an overall sensitivity 339.956 pm/MPa. Applications include mining engineering, petroleum pipeline, natural gas industry, and civil engineering.

Table 2: FBG-Diaphragm Pressure Sensor Comparison

Concept	Sensitivity	Range	Diaphragm Material (E, υ)	Radius to Thickness Ratio	Diaphragm Fixture Method	Temperature Compensation	Authors
Dual-FBG Diaphragm Pressure Sensor	1.57 pm/kPa	0 to 1 MPa	304 Stainless Steel (193 GPa, 0.31)	20	Weld	Yes	Huang et al. [19]
Highly Sensitive FBG Diaphragm Pressure Sensor	0.116 nm/kPa	0 to 15 kPa	Rubber (1.4 MPa, 0.19)	112	Undisclosed	No	Allwood et al. [20]
Liquid level measurement based on FBG-embedded diaphragm	2.8 pm/mm H_2O	50 to 500 mm H_2O	Epoxy Resin (1.6 MPa, 0.47)	8.64	Retainer Ring	Yes	Díaz et al. [22]
Liquid level monitoring system utilizing polymer fibre	57.3 pm/cm H_2O	0 to 75 cm H_2O	Epoxy Resin (1.6 MPa, 0.47)	22.73	Retainer Ring	No	Marques et al. [21]
A fibre bragg grating pressure sensor with temperature compensation based on diaphragm-cantilever structure	339.956 pm/MPa	0 to 10 MPa	304 stainless steel (193 GPA	2	Retainer Ring	Yes	Liang et al. [23]

Based on the existing literature examined across related journals and databases, several FBG-Diaphragm pressure sensors have been developed for various ranges and applications. However, there is an absence of FBG-Diaphragm sensors that have the capability to detect within the range of centimetres of water while being exposed to pressures that are four orders of magnitude or greater than the resolution. The sensors developed by Marques et al. and Liang et al. are within the same order of magnitude as the target resolution set however function at low operating pressures.

1.4 Pressure compensation in ocean-bottom pressure sensors and hydrophones

Pressure compensation is the application of a mechanism which allows a sensor to operate and be insensitive to hydrostatic pressure above a given threshold. This would allow a sensor to be sensitive to 1 cmH_2O with a hydrostatic pressure of 2500 mH_2O, as this is the target for this thesis.

Pressure compensation has been reported in the literature on hydrophones and bottom pressure sensors. A pressure compensated hydrophone is described [25], which adopts a type of slider that changes a chamber's volume proportionally to operating depth. The design of this sensor can be seen in Figure 6.

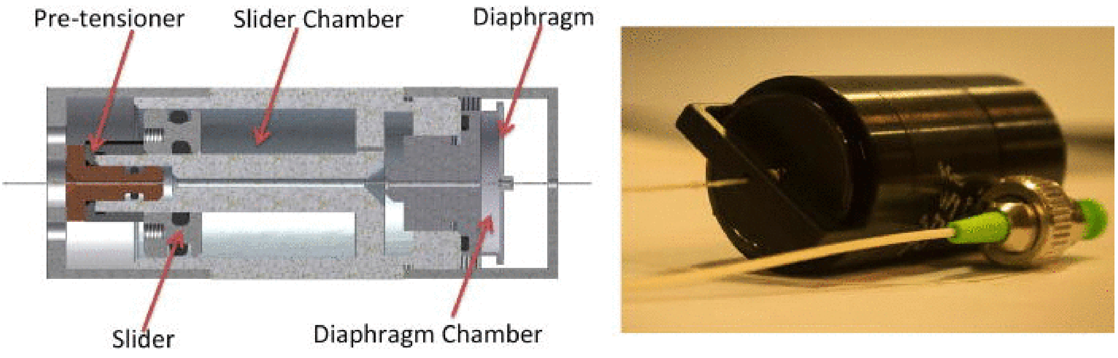

Figure 6: Pressure compensated hydrophone Chandrika et al. [25]. Image reprinted with permission from AIP publishing.

The sensitivity is not affected by this pressure compensation mechanism with the use of a low-pass filter that connects the air chamber behind the diaphragm and slider chamber, thereby allowing only low frequency changes into the diaphragm chamber [25].

Pressure compensation technique for an ocean bottom pressure meter is developed in [26] similarly to the previously discussed method. A schematic of the inner works of this pressure meter is illustrated in Figure 7.

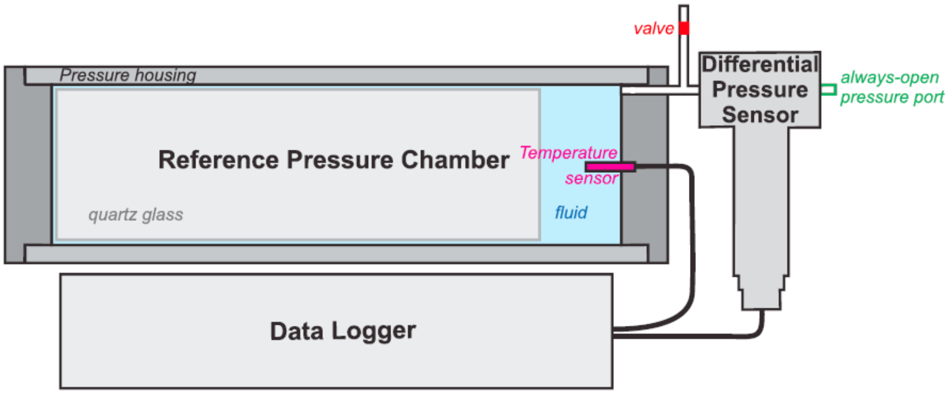

Figure 7: Pressure compensated ocean bottom pressure meter [26]. Image reprinted with permission from John Wiley and Sons publishing.

A reference pressure chamber constructed of quartz glass is contained in a housing that also holds a fluid. A differential pressure sensor provides signal associated to the differential pressure of the internal pressure of the housing and the external pressure of the surrounding ocean.

1.5 Motivation

The motivation of this work is to propose a viable pressure sensor as an inexpensive alternative to commercial sensors with comparable operating specifications, on a cost per unit basis and required accessory equipment expenses. As summarized in Section 1.2, commercial models range in price from $3,400 to $10,475 USD whereas the proposed design cost for a single sensor should fall significantly below the lower figure. The second opportunity in cost savings can be derived by deploying multiple sensors within an array. Through the incorporation of multiplexed FBGs, up to 128 FBGs or 64 temperature-referenced sensors could be embedded in a single fibre cable with a combination of wavelength division multiplexing and spatial division multiplexing (SDM) [27]. Figure 8 illustrates the fundamental principles of multiplexing and how it could apply to ocean sensors.

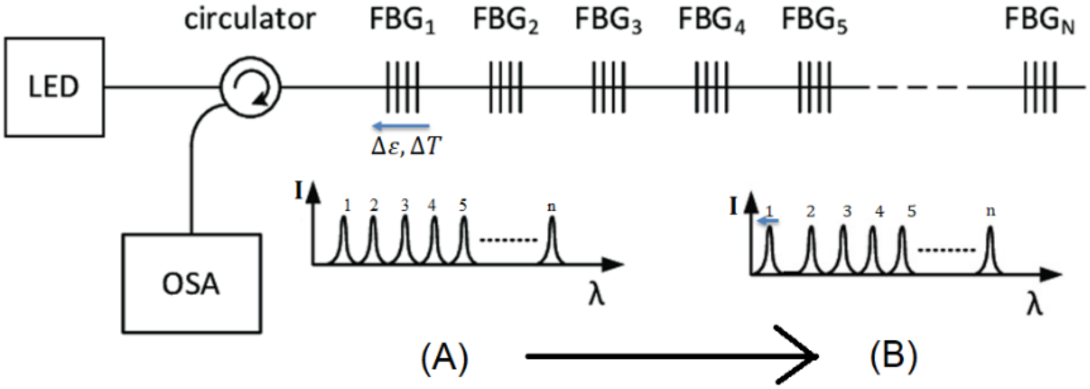

Figure 8: Multiplexing of FBGs. An array of FBGs are embedded along a single fibre that feeds into one acquisition system. In this case, an LED provides the light source while the Optical Spectrum Analyzer (OSA) interprets a signal. Each FBG has an associated Bragg wavelength peak shown in spectra A and B. If FBG_1 is perturbed by a change in surrounding temperature or strain, the Bragg wavelength peak associated with FBG_1 will shift accordingly irrespective of the other FBG Bragg wavelengths. This is portrayed in the translation of peak 1 in wavelength between spectrum A and spectrum B.

If each sensor instrumented with an FBG is positioned in an array to form a monitoring system; in practice these FBGs could all relay back to a single interrogation unit rather than multiple units. This would drive the overall cost per deployed sensor down and scale as more sensors are added. Conversely, electrical signal-based sensors are generally monitored by a proprietary recorder or shared with other sensors on a 4-channel recorder and therefore do not allow for scalable cost reduction. The use of FBG-based pressure sensors could reduce a portion of costs that are otherwise incurred by electrical signal-based sensors and their auxiliary equipment required. It must also be acknowledged that substantial costs are incurred through the use of oceanographic vessels used to deploy ocean sensors, which can upwards of $20,000 per day [28]. However, the reduction in capital costs can be beneficial and improve the viability of oceanographic monitoring endeavours.

1.6 Objective

The objective of this research is to develop and test a design concept for a deep-ocean pressure sensor based on an FBG fixed to a diaphragm and that includes a method of pressure compensation. The main limitations observed from commercial sensors of a similar nature to the proposed design is namely cost. The potential role of pressure compensation when designing a pressure sensor is to allow high sensitivity at high ambient pressures, a feature that is crucial for tsunami and vertical seafloor deformation detecting. The key benefit of employing FBGs is that multiple sensors could be multiplexed on a single optical fibre to enable dispersed measurements of ocean bottom pressure with a single interrogation system, thus reducing cost per installed sensor. A diaphragm was selected as a transducing component due to the linearity it offers and it being well suited to be mounted on cylindrical enclosures. Granted this, the goal of this thesis is to develop an FBG & diaphragm-based bottom pressure sensor concept with pressure compensation allowing for a resolution of 1 cmH_2O and an operating range of up to 2500 mH_2O.

1.7 Overview

This thesis is presented in six chapters, as follows:

Chapter 2 outlines basic information on the mechanics of diaphragms and operating principles of FBGs.

Chapter 3 opens by exhibiting a potential full-scale sensor design, outlining the operating principles and mechanisms to facilitate a sensitivity to water column changes.

The theory applied to create the design is reviewed in detail with the gradual manipulation of expressions accompanied by an explanation of their relevance.

Chapter 4 examines the practical purposes of the thesis and describes the experimental configurations and conditions of testing.

Chapter 5 reviews the results produced with the experimental validation of the sensor's sensitivity and the FEA findings.

Chapter 6 discusses the conclusion of the thesis and provides insight into the considerations and undertakings to be made in future work.

Chapter 2 - Diaphragm and FBG mechanical principles

2.0 Introduction

This Chapter presents background detail on key aspects of the sensor design. First, relations describing deflection and strain in pressure-loaded diaphragms are presented. Second, operating principles of FBGs and the expressions that describe their behaviour are introduced.

2.1 Fundamentals of diaphragms and small deflection theory

A diaphragm can be characterized as a thin sheet of flexible material with a high diameter-to-thickness ratio and a geometric shape that is, most commonly, circular. Depending on the application, the exposed face of a diaphragm is usually flat and, in some applications, is corrugated [29]. A diaphragm is generally fixed about its periphery.

Analysis of the behaviour of diaphragms under pressure is performed using small deflection theory for thin uniform plates [12] which assumes that the mid-plane of the diaphragm, found midway between the top and bottom surfaces, is unstressed. Biaxial stress in the plane of the diaphragm occurs elsewhere in the diaphragm. Three possible boundary conditions can be assessed: free, guided (zero slope but free to move axially), and fixed [30]. For analysis presented here, only the fixed support case with an evenly distributed load surface of a circular plate will be considered. Outlined below are the equations that apply to the design a diaphragm-based sensor under these conditions.

A diagram including the geometric notation describes a diaphragm in deflection, as seen in Figure 9.

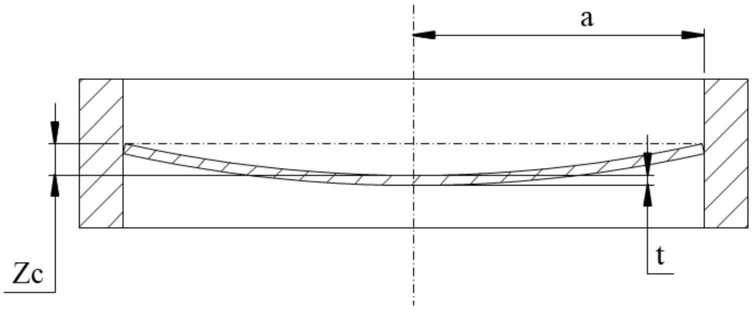

Figure 9: Diaphragm in deflection with geometric notation.

The deflection, z, centre deflection, z_c, centre stress, σ_c, and centre strain ε_c for diaphragm with uniformly distributed pressure, q, and fixed peripheral support are calculated as follows [30] [31].

$$z = \frac{3qa^4(1-v^2)}{16Et^3}\left[1-\left(\frac{r}{a}\right)^2\right]^2 \tag{2.1}$$

$$z_c = \frac{3qa^4(1-v^2)}{16Et^3} \tag{2.2}$$

$$\sigma_c = \frac{3qa^2(1+v)}{8t^2} \tag{2.3}$$

$$\varepsilon_c = \frac{1}{E}\big(\sigma_c(1-v)\big) \tag{2.4}$$

In these expressions, q is the load per unit area, a is the radius of the diaphragm, v is Poisson's Ratio, E is Young's Modulus, r is the radial coordinate, and t is the thickness of the diaphragm.

Substituting Equation (2.1) into Equation (2.4) yields:

$$\varepsilon_c = \frac{3qa^2(1-v^2)}{8Et^2} \tag{2.5}$$

Equation (2.1) allows the calculation of the deflection for a given radial coordinate which is useful for determining the volume swept based on a given applied distributed load. Equation (2.3) is the bidirectional stress that forms at the centre of the diaphragm for a given applied distributed load which gives way to the strain at the centre. At the centre of a diaphragm, the tangential and radial components for both stress and strain are equal to one another.

The diaphragm also has an inherent linear operating range that is based on guidelines defined by [30]. It states that in order for linearity to be safely assumed, the centre deflection, defined in this thesis as z_c, must not exceed a maximum length equal to half of the diaphragms thickness.

2.2 Fibre Bragg grating principles

The sensing element of a typical diaphragm-based sensor is a resistive strain gauge which, typically, is bonded to the diaphragm. However, an FBG can be used instead of a strain gauge in a diaphragm-based pressure sensor. As described in Chapter 1, the benefits of this approach include a resistance to electromagnetic interference and the capability for multiplexing allowing multiple FBGs along a single fibre core. In this section, the operating principles of an FBG are described.

Fibre Bragg gratings (FBG) are periodic variations in the index of refraction of the core of an optical fiber. An FBG allows transmission of the majority of the spectrum of the incoming light but a small band, centred at the Bragg wavelength is reflected back toward the source (Figure 10). The Bragg wavelength varies in response to external physical inputs such as temperature and strain. An illustration of an FBG structure along with the core refractive index profile and spectral response is seen in Figure 10.

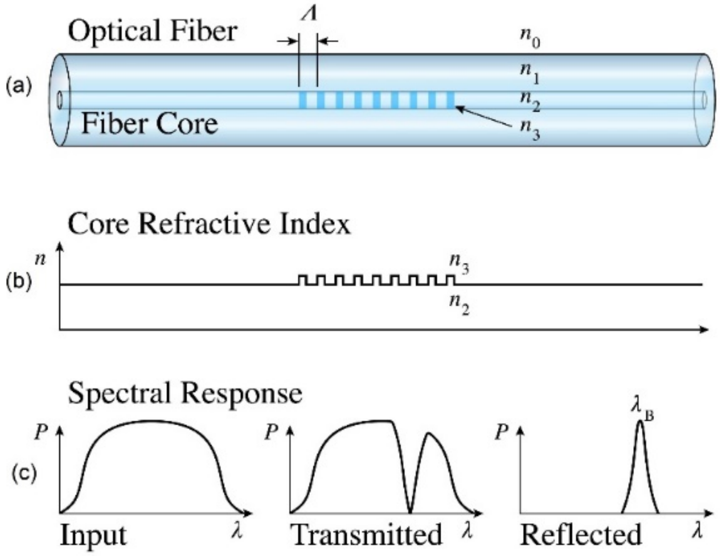

Figure 10: FBG Fundamental Aspects. A fibre core embedded with Bragg gratings is seen in (a). The core refractive index is shown in (b). The spectral response is seen in (c) describes the function of a Bragg gratings. Image was created by Sakurambo and reprinted from Wikipedia [32].

The component within a spectrum of optical light which is reflected, the Bragg wavelength (λ_B), is expressed as:

$$\lambda_B = 2n_{eff}\Lambda \tag{2.6}$$

where n_{eff} is the effective refractive index of the grating and Λ is the grating periodicity [33]. The Bragg wavelength is an important parameter, as light at this wavelength forms the basis of what is to be detected be interrogators for sensing applications.

Axial strain applied to an FBG, at a constant temperature, will cause a change in the grating spacing (Λ) and photoelastic-induced change in the effective refractive index

(n_{eff}) of the fibre both of which contribute to a shift in the Bragg wavelength (λ_B) [33]. The shift in Bragg wavelength ($\Delta\lambda_B$) for a given axial strain (when ΔT=0) is expressed as shown in Equation 2.7 [33].

$$\Delta\lambda_B = \lambda_B(1 - P_e)\Delta\varepsilon_z \tag{2.7}$$

where

$$P_e = \left(\frac{n_{eff}^2}{2}\right)[p_{12} - \upsilon(p_{11} + p_{12})] \tag{2.8}$$

where, p_{11} and p_{12} are Pockel's coefficients of the strain-optical tensor, υ is the material Poisson's ratio of the optical fibre. $\Delta\varepsilon_z$ is the applied longitudinal strain. For a standard single-mode germanosilicate optical fibre, the values typically used are: p_{11} = 0.113, p_{12} = 0.252, ν = 0.16, and n_{eff} = 0.148. For a grating with a Bragg wavelength centred at 1550 nm, Equation 2.7 predicts a strain sensitivity of 1.2 pm/με [33].

Equation (2.7) excludes the thermal effects when stable temperatures conditions exist however should be accounted for in the presence environments where temperature changes are expected. In the absence of strain ($\Delta\varepsilon_z = 0$) the change in Bragg wavelength with respect to a change in temperature (ΔT) is expressed by Sengupta [33] is stated as

$$\Delta\lambda_B = \lambda_B(\alpha + \delta)\Delta T \tag{2.9}$$

The thermal expansion coefficient of the fibre is α and the thermo-optic coefficient is δ. For an FBG with Bragg wavelength centred at approximately 1550 nm, one can expect to see a temperature response of 13 pm/°C [33].

This dual-sensitivity can create complications for sensor development however this can be corrected by including an additional FBG independent of strain to serve as a temperature reference. Readings taken from a secondary FBG allows the sensor operator to cross reference the change and compensate for the thermal effects occurring in the strain sensing FBG [33]. Alternatively, one can place a temperature probe within proximity of a strain sensing FBG to gather a temperature measurement and account for any temperature changes as the collected data is processed.

By using FBGs for temperature or strain sensing devices, a host of advantages can be gained over other means of sensing such as piezoresistive or piezoelectric methods. The main advantages, as noted by Sengupta [33] are:

1. FBG sensors are contained in a small size
2. The passive components operate for long lifetimes.
3. Fibre optic cables operate with little losses which allows transmission of signals over tens of kilometres.
4. In the presence of electromagnetic radiation, FBGs do not experience interference and can operate in harsh environments where regular sensors generally fail.
5. The lack of electrical signals renders FBGs suitable for environments with explosion hazards.
6. When multiple sensors are required, several FBGs can be multiplexed along one optical fibre reducing the cost of complex control systems and increasing the ease of implementation.

It is also worth noting that there are some drawbacks to using FBGs. Most commonly, optical fibre is made of germanosilicate glass and is, therefore, fragile. Another drawback is that the light source and interrogation systems needed to use FBGs are more expensive than data acquisition systems for electrical signals. Nonetheless, for some applications, the advantages of FBGs outweigh the drawbacks.

Chapter 3 - Sensor design, analysis and examples

3.0 Introduction

This chapter presents the conceptual design of a full scale working FBG-Diaphragm-based ocean bottom pressure sensor for high-resolution measurements. The design includes a method of pressure compensation that limits the differential pressure to which the diaphragm is exposed, independent of the ambient pressure. A device description is provided with drawings that illustrate fundamental components accompanied by a discussion of the working principles. This is followed by the of derivation of a theoretical model of sensor operation which is used to assess alternative device configuration.

3.1 Design concept

The design comprises a cylindrical pressure vessel fitted with a moveable piston and a diaphragm, as shown in Figure 11, which create Chambers A and Chamber B, within the vessel. The diaphragm is instrumented with an FBG, not shown in the figure, and the associated change in Bragg wavelength is used to determine the magnitude of changes in the pressure difference across the diaphragm.

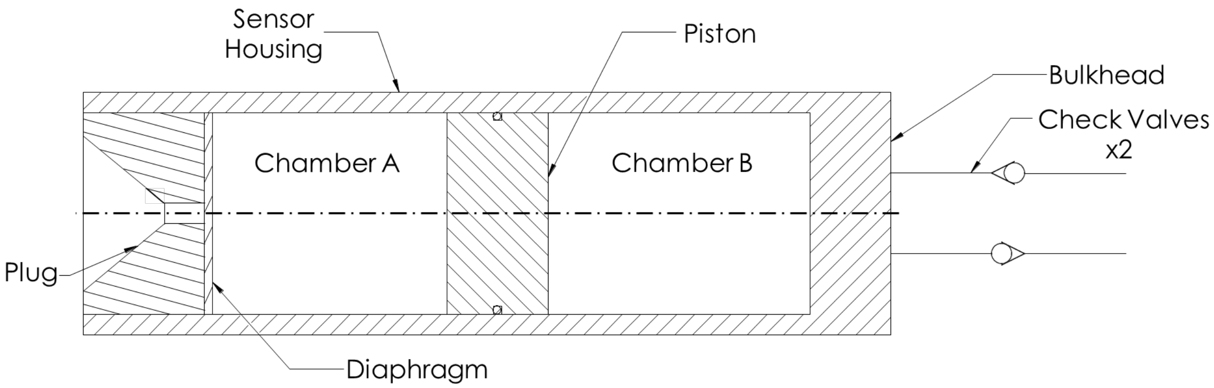

Figure 11: Sensor design concept

The diaphragm is anchored and sealed to the inner wall of the vessel and is supported on its external side by a plug to ensure its survival when the pressure in Chamber A exceeds ambient pressure. A small hole in the plug ensures that the ambient pressure is in communication with the diaphragm. Chamber B is connected to ambient pressure via two lines, each of which includes a one-way check valve. Chamber A is filled with a compressible gas that is pressurized prior to or during sensor deployment.

Figure 12 illustrates the three primary operational states of the sensor which is of a unique design.

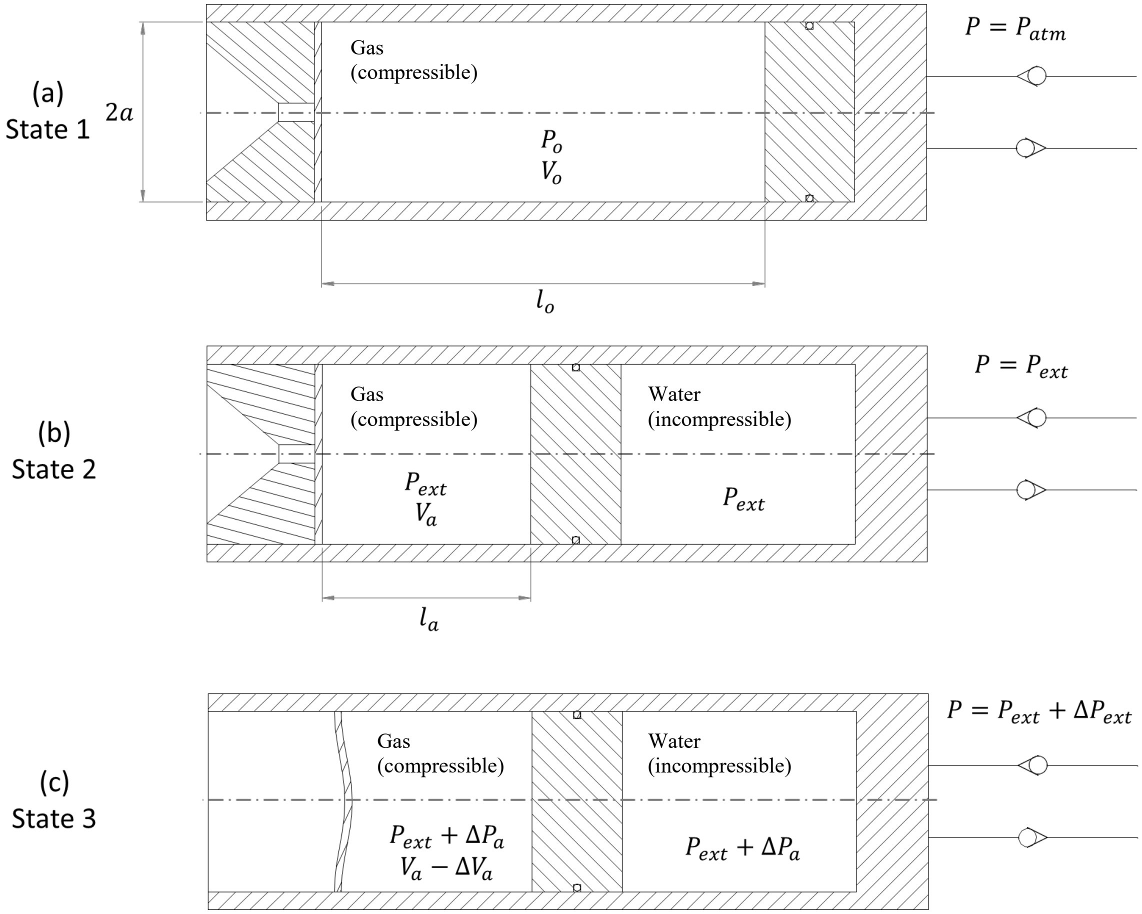

Figure 12: Diaphragm Pressure Sensor operating states: (a) State 1 - before deployment with external pressure equal to atmospheric pressure; (b) State 2 - at the target depth; (c) State 3 – at target depth with a change in external pressure.

In State 1, prior to deployment, Chamber A is filled with a compressible gas at pressure, P_o, referred to as the preload, which is significantly higher than atmospheric pressure. Chamber B is at ambient pressure which is equal to atmospheric pressure. As a result of the pressure difference between Chambers A and B, the piston is in the extreme right-hand position.

In State 2, the sensor is deployed at a target depth where P_{ext} exceeds P_o. In moving from State 1 to State 2, water is admitted to Chamber B via the lower check valve leading to further compression of the gas in Chamber A. This occurs when the instantaneous ambient pressure from hydrostatic pressure surpasses P_o in Chamber A. Chamber B continues to fill until the sensor has reached the intended depth for monitoring.

In State 3, pressure external to the sensor at the target depth has increase by ΔP_{ext}. This change does not exceed the cracking pressure of the check valves and thereby maintains isolation between Chamber B and the external ambient expanse. This pressure change causes the diaphragm to deflect to the right which, in turn, reduces the volume of Chamber A by ΔV_a. The resulting reduction in volume induces a pressure increase of ΔP_a in both Chamber A and B. Note that it is assumed that the water in Chamber B is incompressible and, therefore, the diaphragm deflection does not cause any change in volume of Chamber B. As described earlier, the diaphragm is instrumented with an FBG and the associated change in Bragg wavelength is used to determine the magnitude of ΔP_{ext}.

To ensure that the sensor is sensitive to both positive and negative changes in external pressure, in its the neutral position (i.e. for ΔP_{ext}=0), the plug is disengaged, as shown schematically in Figure 4(c). This can be achieved by applying using a soluble plug material or incorporating some disengagement mechanism with corroding links.

3.2 Analysis

In this section, relations are developed that are used to analyse the performance of the sensor design shown in Figure 4.

This analysis assumes that the compressible gas in Chamber A behaves in accordance with the ideal gas law:

$$PV = mRT \tag{3.1}$$

Here, P is pressure, V is volume, m is mass, R is the specific gas constant, and T is temperature. This expression is valid under the assumption that the compressibility factor ($Z = \frac{PV}{mRT}$) is approximately unity. Within the range of pressures from 5 MPa (~510 mH_2O) to 25 MPa (2550 mH_2O) at a temperature of 275 °K, the compressibility factor remains within 5% [34]. The target depth of 2500 mH_2O was selected with cognizance of this constraint.

The diagrams shown in Figure 12 define the variables used to derive the theoretical model showcased in Section 3.3. The functions ΔP_a and ΔV_a with their respective independent input variables P_{ext}, V_a, and ΔP_{ext}, are outlined in the following passages.

If there is no change in mass ($m_i = m_f$) and assuming constant temperature ($T_i = T_f$) from an initial to final state, the ideal gas law is used to describe this two-stage process involving solely pressure and volume changes as follows:

$$P_i V_i = P_f V_f \tag{3.2}$$

This expression forms the basis for selecting the dimensions of the sensor body and the test conditions under which to test it. With the adoption of Equation (3.2), parameters of State 2 of Figure 12 (b) are considered initial (1) whereas parameters of State 3 of Figure 12 (c) are final (2) and thus are related as:

$$P_{ext} V_a = (P_{ext} + \Delta P_a)(V_a - \Delta V_a) \tag{3.3}$$

The magnitude of ΔV_a is equal to the volume under the deflected diaphragm, as shown in Figure 5, whose shape is defined in part by Equation (2.1) (Chapter 2). This volume can be expressed as the integral shown in Equation (3.4).

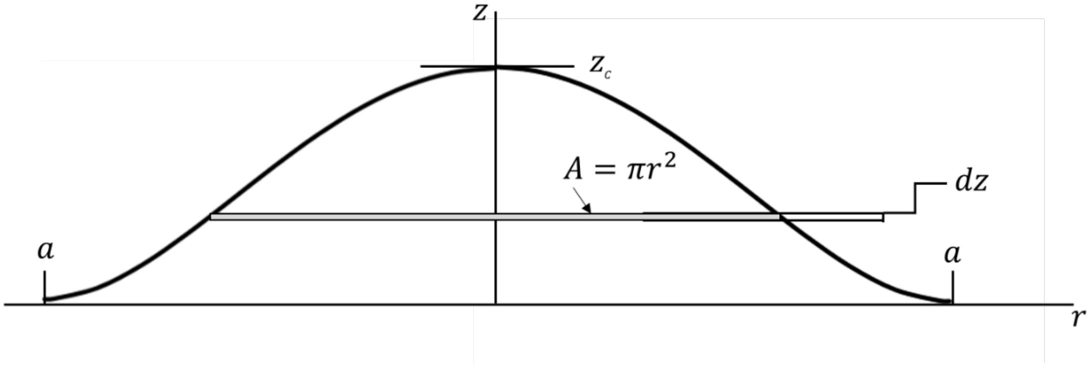

Figure 13: Deflection profile of a diaphragm fixed at the edges with a distributed load.

$$\Delta V_a = \int_0^{z_c} \pi r^2 dz \tag{3.4}$$

An expression for the radius, r, can be determined from Equation (2.1), as follows.

$$r = a\sqrt{1 - \sqrt{\frac{z}{z_c}}} \tag{3.5}$$

Substituting Equation (3.5) into Equation (3.4), the volume swept for a deflected diaphragm is restated as:

$$\Delta V_a = \int_0^{z_c} \pi a^2 \left(1 - \sqrt{\frac{z}{z_c}}\right) dz \tag{3.6}$$

Computing the integral and substituting in Equation (2.1) yields:

$$\Delta V_a = \frac{\pi q a^6(1-\nu^2)}{16Et^3} \tag{3.7}$$

The load, q, is the pressure difference across the diaphragm, $\Delta P_{ext} - \Delta P_a$.

$$\Delta V_a = \frac{\pi(\Delta P_{ext} - \Delta P_a)a^6(1-\nu^2)}{16Et^3} \tag{3.8}$$

The volume of Chamber A, V_a, is,

$$V_a = \pi a^2 l_a \tag{3.9}$$

where l_a is the length of the Chamber A.

Using Equation (3.2), l_a is defined as:

$$l_a = \left(\frac{P_{atm} + P_o}{P_{ext}}\right) l_o \tag{3.10}$$

where P_{atm} is atmospheric pressure (101 kPa).

Inserting Equations (3.7), (3.8), and (3.10) into Equation (3.3), yields a quadratic expression for ΔP_a that simplifies to:

$$\Delta P_a^2 + \left(P_{ext} - \Delta P_{ext} + \frac{16Et^3 l_a}{a^4(1-\nu^2)}\right)\Delta P_a - P_{ext}\Delta P_{ext} = 0 \tag{3.11}$$

This equation can be solved using a quadratic equation formula or a roots computing function (See Appendix A).

Taking Equation (2.5) and substituting $q = \Delta P_{ext} - \Delta P_a$ yields,

$$\varepsilon = \frac{3(\Delta P_{ext} - \Delta P_a\ )a^2(1-\nu^2)}{8t} \tag{3.12}$$

Where ε is the in-plane strain at the centre of the diaphragm This expression can be differentiated with respect to the applied pressure ΔP_{ext},

$$\frac{d\varepsilon}{d\Delta P_{ext}} = \frac{d}{d\Delta P_{ext}}\left(\frac{3(\Delta P_{ext} - \Delta P_a)a^2(1 - \nu^2)}{8Et^2}\right) \tag{3.13}$$

Lastly, the differentiated form of Equation (2.7),

$$\frac{d\lambda_B}{d\varepsilon} = \lambda_B(1 - P_e) \tag{3.14}$$

is used to eliminate $d\varepsilon$,

$$\frac{d\lambda_B}{d\varepsilon} * \frac{d\varepsilon}{d\Delta P_{ext}} = \frac{d\lambda_B}{d\Delta P_{ext}} \tag{3.15}$$

thereby yielding:

$$\frac{d\lambda_B}{d\Delta P_{ext}} = \lambda_B(1 - P_e)\frac{d}{d\Delta P_{ext}}\left(\frac{3(\Delta P_{ext} - \Delta P_a\ )a^2(1 - \nu^2)}{8Et^2}\right) \tag{3.16}$$

This expression provides the sensor sensitivity in terms of Bragg wavelength shift for a given change in the external pressure. Please see the Appendix for the full written form of Equation (3.16).

3.3 Sensor design examples

In this section, possible design configurations for three different ocean depths (i.e. 500 m and 2500 m) are explored. The operating pressure, P_{ext}, is defined as

$$P_{ext} = \rho g h \tag{3.17}$$

where ρ is the density of sea water, g is acceleration due to gravity, and h is the depth of deployment.

The Young's Modulus (E) and Poisson's Ratio (υ) for the diaphragm material are 198 GPa and 0.27, respectively, are based on the characteristics of 316 Stainless Steel. The controllable variables of the model are diaphragm thickness (t), diaphragm diameter (a), initial chamber length (l_o), and preload pressure (P_0). Preload pressure is described as function of P_{ext} and a preload factor k, ranging from 0 to 1:

$$P_0 = kP_{ext} \tag{3.18}$$

Using Equations (3.16), a set of graphs are generated for two deployment scenarios. The first type of graph shows sensitivity as a function of diaphragm thickness across a set of diaphragm diameters, while holding a l_o and k constant. The second graph shows sensitivity as a function of preload factor for a set of sensor housing lengths while maintaining constant diaphragm properties (a, t). A final graph is produced to demonstrate sensitivity varying for depths of up to 2500 mH_2O.

3.3.1 Sensor configuration for 500m of depth

An ocean depth of 500 m provides hydrostatic pressure that would be found in relatively close proximity to coast lines. While this depth would not be ideal for a tsunami detection system, one might use a sensor at this depth for monitoring vertical seafloor deformation.

In Figure 14, modelled sensitivity is plotted as a function of diaphragm thickness and diameter appropriate for this depth.

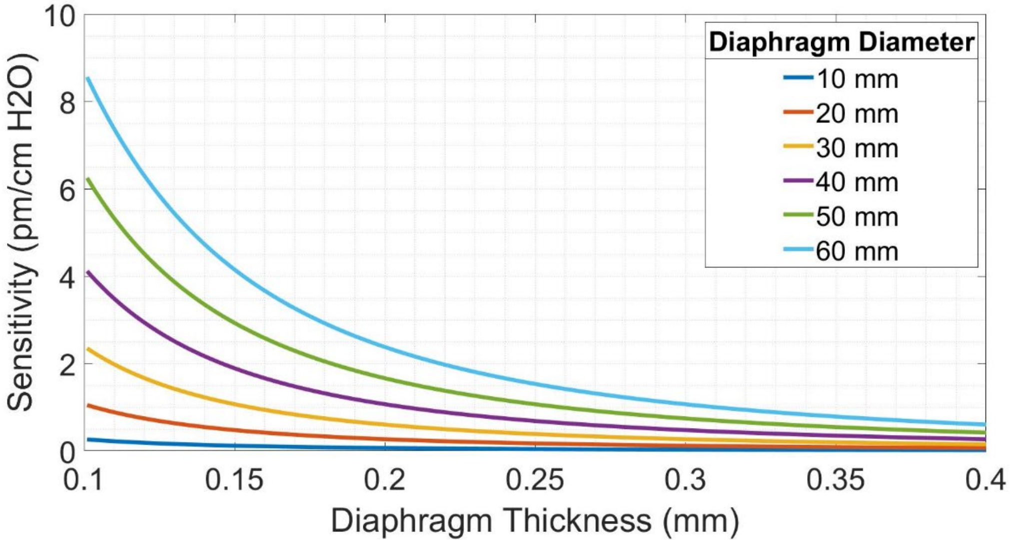

Figure 14: Sensor sensitivity as a function of varying diaphragm thickness for a set of diaphragm diameters at a target depth of 500 m. The length of the housing is defined as 150mm long and the initial internal preload factor is 75% of the target depth pressure. Developed with Script 1 (seen in Appendix A).

Diaphragm diameter varies from 10 mm to 60 mm and diaphragm thicknesses ranges from 0.1 mm to 0.4 mm. As expected, sensitivity rapidly decreases as thickness increases, whereas sensitivity is higher at larger diaphragm diameters. A thicker diaphragm will tend to strain less as more material opposes the same applied load. Conversely, a larger diameter will cause a greater bending moment for a given load and therefore will strain more than smaller diameters. These two parameters, thickness and diameter are proportional, such that if one is raised the other must also be raised to maintain a constant sensitivity. If the thickness and diameter are doubled, the sensitivity remains nearly identical. For reference, the diaphragm specifications of thickness and diameter of the lab-tested sensor are 0.15mm and 50mm respectively. Given the lengths and preload selected for the model, the sensitivity would be 2.9 pm/cmH$_2$O.

In Figure 15, modelled sensitivity is plotted as a function of sensor length and pressure preload.

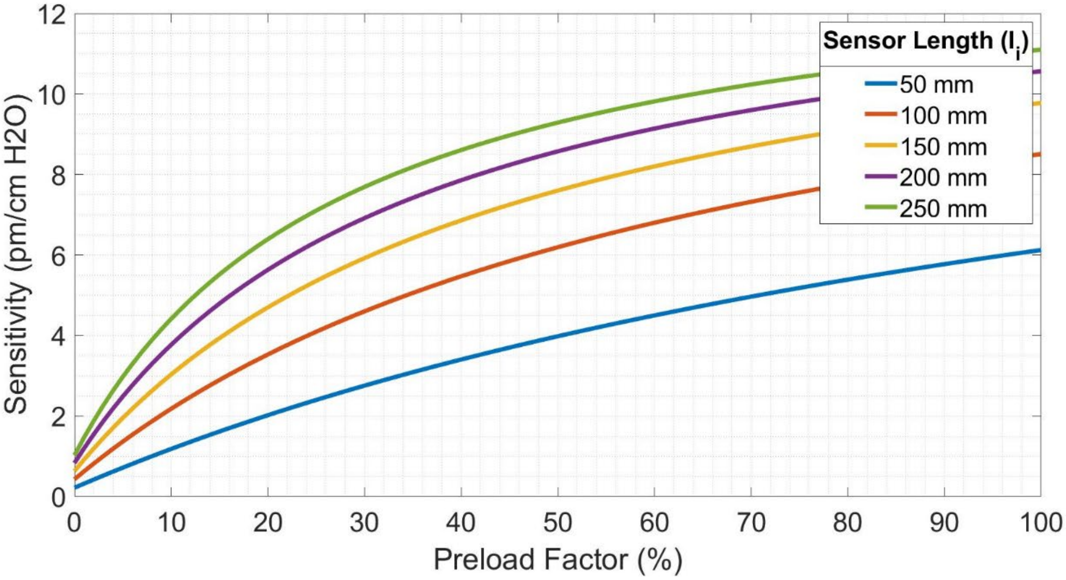

Figure 15: Sensor sensitivity as a function of varying preload factor for a set of sensor housing lengths at a target depth of 500 m. The diaphragm diameter and thickness set are 50 mm and 0.15 mm respectively. Developed with Script 2 (seen in Appendix A).

The plot that is produced is inversely profiled compared to that of Figure 14. As expected, when both preload factor and sensor length increase, theoretical sensitivity increases however at diminishing returns. With longer sensor lengths, the effects of preloading the sensor are more pronounced initially then level off asymptotically at a certain sensitivity as seen in Figure 15. Considering this, one would select a configuration that either has a short sensor length and a high preload factor such as 50 mm and 80% respectively to achieve a sensitivity of 5.4 pm/cmH$_2$O. Conversely one might opt for long sensor length and low preload such as a length of 250mm and a k of 15% to produce a similar sensitivity.

3.3.2 Sensor configuration for 2500m of depth

The final case examined for the numerical model is with a target depth of 2500m, or approximately 245 bars. The DART stations found throughout global tsunami monitoring projects are typically deployed between 1500-6000m, so 2500m would represent the lower-middle range of what might be deployed in such systems [8]. At a depth of 2500m, the associated pressure is still within a reasonable compressibility factor such that the use of ideal gas law is still appropriate. Given the higher hydrostatic pressure, the theoretical sensor design had to increase preload pressure to allow a similar sensitivity of the previous case to be obtainable.

In this configuration, the model has the housing length and preload factor set to 150mm and 75% respectively across ranging diaphragm diameters and thicknesses as is seen in Figure 16.

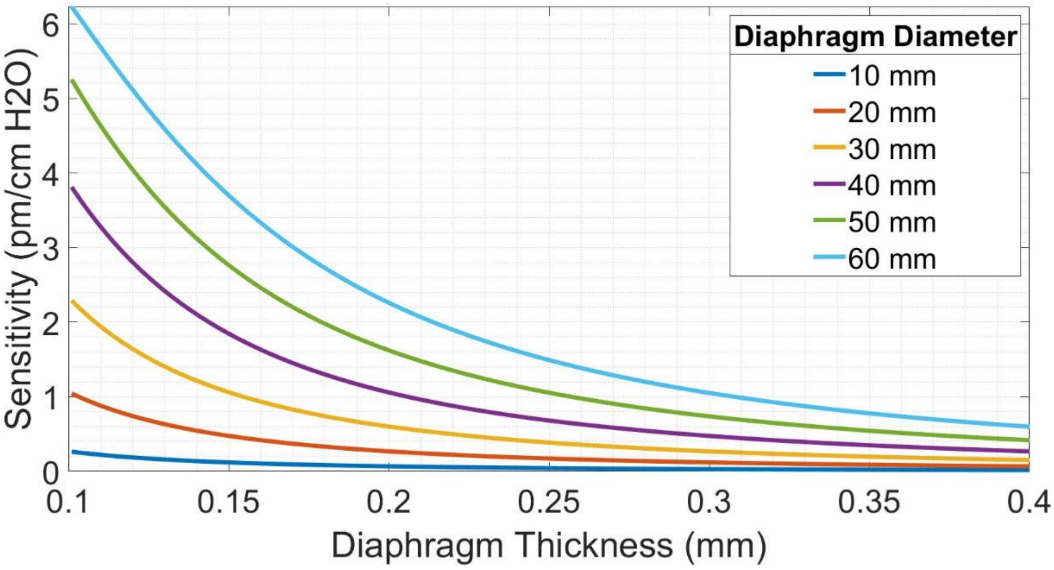

Figure 16: Sensor sensitivity as a function of varying diaphragm thickness for a set of diaphragm diameters at a target depth of 2500 m. The length of the housing is defined as 150mm long and the initial internal preload factor is 75% of the target depth pressure.

Overall, the magnitude of sensitivities has dropped when comparing Figure 14 at 500m of depth and Figure 16 at 2500m of depth. This is to be expected as a greater depth imparts a higher pressure in Chamber A which in turn creates more of a resistance to the diaphragm when deflecting and thus results in a lower strain.

In Figure 17, a comparison of sensitivity to preload factor is made across a range of sensor lengths while holding a constant diaphragm diameter and thickness.

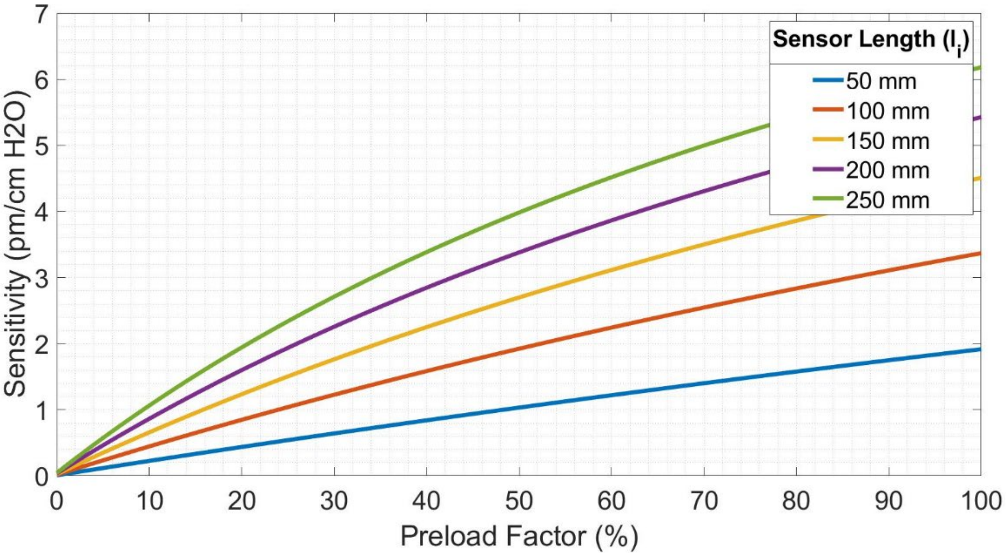

Figure 17: Sensor sensitivity as a function of varying preload factor for a set of sensor housing lengths at a target depth of 2500 m. The diaphragm diameter and thickness set are 50 mm and 0.15 mm respectively.

At a higher target depth, the sensitivity curves are less accentuated as preload factor increases. Thus, it is deduced that the preload factor applied merits more consideration when testing at lower depths.

3.3.3 Sensitivity with a varying target depth

In the scenario that a different target depth to the original depth is applied, Figure 18 could be used to determine the sensitivity of an already constructed sensor. The geometry and materials are closely based to the experimental sensor developed in Chapter 4.

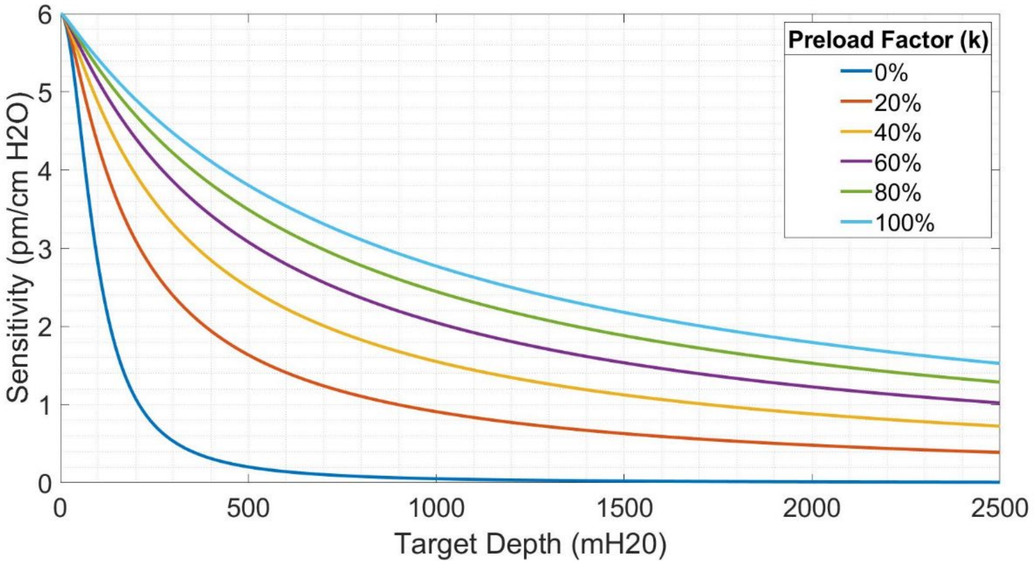

Figure 18: Sensitivity as a function of target depth across a range of preload factors from 0-100%. Diaphragm diameter and thickness are 50mm and 0.15mm respectively and a sensor length of 30mm. Developed with Script 3 (seen in Appendix A).

Intuitively, an increasing target depth will result in a decreased sensitivity which can be counteracted by increasing the preload factor. The experimental sensor has a preload factor curve of 0% so one would refer to the dark blue plot. Based on this set characteristics, such a sensor would only be feasible for depths not exceeding 200m. The sensor built is tested at depth pressures that do not exceed 50 mH_2O based on laboratory and instrument limitations. The sensitivity examined here is between 5-6 pm/cmH_2O as seen in Figure 18.

3.4 Summary

A design concept is proposed as what could be a full-scale ocean deployable sensor with a preliminary consideration for the components that would provide a working mechanism for pressure equilibration and measurement. The essential components that act to transduce pressure as changes of the water column to a detectable signal are a diaphragm and Fibre Bragg Grating. With an outlined design concept, the theoretical principles that form the basis for a numerical model are manipulated to describe each aspect of the sensor design to ultimately produce a theoretical sensitivity based on an applied pressure. Lastly, the numerical model representing the proposed design concept is utilized to present two possible deployment cases at 500m and 2500m of ocean depth. A family of curves for each deployment depth is generated showing sensitivity with respect to diaphragm thickness and diameter. The main takeaways from the model are that as diameter increases or thickness decreases, sensitivity will increase. Furthermore, at higher testing depths, sensitivity will tend to decrease which can be compensated by increasing sensor housing length and/or initial preload pressure. The model is limited by the capacity of Ideal Gas law to function under a constrained temperature and pressure range. From a solid mechanic perspective, the diaphragm has a limited linearity range for which deflection can occur. Given these considerations, future work will likely base the geometric parameters of a working sensor on the outputs provided by this model.

Chapter 4 - Experimental design, methodology, and finite element analysis formulation

4.0 Introduction

In this Chapter, two aspects of the sensor performance are investigated. First, to validate the theoretical model of the sensor developed in Chapter 3, experiments are performed using two custom tests rig in which the diaphragm, instrumented with an FBG, is subjected to a range of differential pressures. Second, a finite element model of the FBG bonded to the diaphragm is developed to assess the effect of the optical fibre on the pressure response of the diaphragm. The methods and results of the pressure tests and of the finite element analysis are presented in this chapter.

4.1 Diaphragm design and fabrication

When considering the diaphragm dimensions and materials, it was essential that the geometry be practical to manufacture, assemble, and use for testing while being capable of generating an adequate sensitivity output. Commercial sensors sizes were used as a point of comparison during the design process of this sensor. In addition, the operation conditions would call for a material that is corrosion-resistant while inexpensive and easily accessible. These considerations resulted in a diaphragm that was manufactured out of 316 stainless steel with a diameter of 5 cm and thickness of 0.152mm.

4.1.1 Design

With the use of the Equation (3.15), a plot is formed to demonstrate the theoretical sensitivity versus target depth pressure for the sensor characteristics seen in Table 8. This plot describes the behaviour of a diaphragm contained within a sensor that is exposed to a target depth pressure of up to 100 psi (70.3 mH_2O) as shown in Figure 19. The x-axis units are labelled in psi as the reference equipment used is incremented in imperial units (for conversion, 1 psi = 0.703 mH_2O).

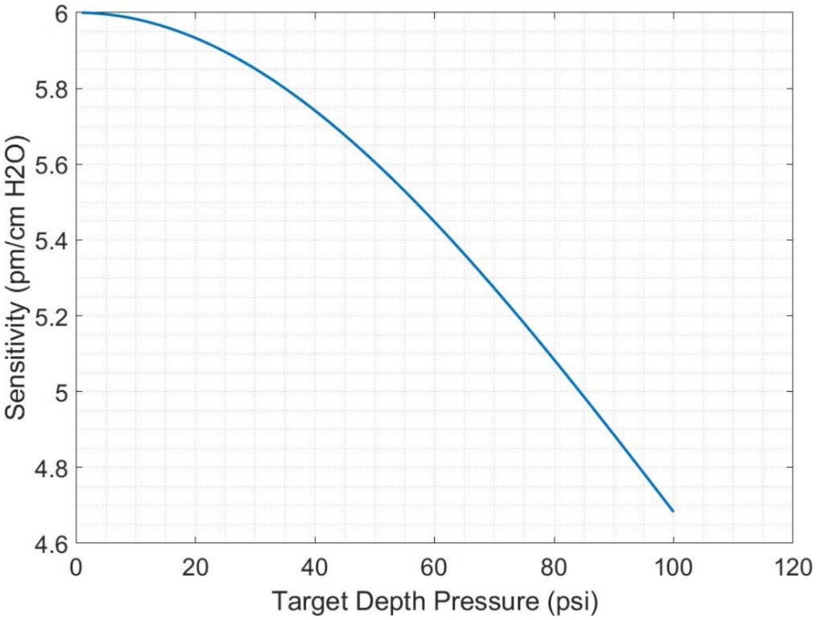

Figure 19: Theoretical sensitivity plot for experimental sensor.

This plot has been developed for comparison the experimental results, presented in Chapter 5.

The theoretical sensitivity is predicted as 6 pm/cmH_2O at atmospheric pressure. This inherent theoretical sensitivity would produce a signal that is discernible by the optical wavelength interrogator while also being within several orders of magnitude smaller than the surrounding system pressures. The interrogator utilized, the Micron Optic sm130, is able to resolve 1pm of change in wavelength, and therefore the associated strain induced to the FBG had to be within the same order of magnitude. It was determined that a factor of 6 be applied to the resolution of the interrogator to provide some bilateral flexibility in possible signal error.

4.1.2 Transducer fabrication

Bonding of the FBG to the diaphragm is a key aspect for the proposed sensor design. A diaphragm is the mechanical component that transduces pressure into strain, thereby amplifying the sensitivity of bonded FBG beyond its relatively low inherent sensitivity to pressure.

A diaphragm is manufactured by taking shim stock sheet of the chosen material type and thickness and cutting it to a selected diameter using a machining lathe. A square cut-out of the shim stock sheet is sandwiched between two cylindrical stocks that are slightly wider than the intended diaphragm diameter and held between the chuck and tailstock of the lathe. As the spindle is revolving, the tool post with a general turning tool makes passes along the edge of stock, trimming the excess material off until the correct radial coordinate corresponding to the desired diameter is achieved. Taking an FBG and manufactured diaphragm, the manner in which these two components are bonded is illustrated in Figure 20.

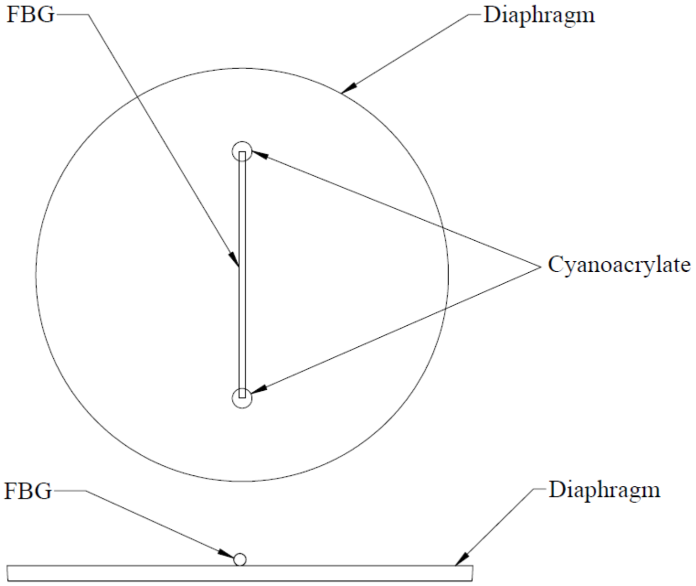

Figure 20: FBG-Diaphragm Sensor Configuration. Diaphragm and FBG not to scale with one another. FBG is shown without the remaining continuous strand of fibre.

The process of bonding involves five simple steps:

i. The centre point diaphragm is marked on its face.

ii. Two additional points are marked collinearly to the center point at a distance equal to the bare fibre length of an FBG. Medium grit sandpaper is applied at these two marked points to create a rougher surface for bonding.

iii. The diaphragm is taped to the table. An FBG is set onto a diaphragm. Aligning the point of the FBG with the bonding point on the diaphragm, a piece of tape is applied to fix one end of the fibre temporarily. A weight such as a paper binding clip is fixed to the other end of the fibre strand and suspended off of the table, placing the fibre in tension. Another piece of tape is applied across the fibre at the other side of the bonding point such that fibre is now completely fixed.

iv. Cyanoacrylate is used as a suitable bonding agent for fibreglass and metallic materials. It is placed onto a separate palette to allow liquid to evaporate leaving a more viscous fluid. With a needle tip, two small droplets are applied to avoid creating disturbances or non-uniformities in the transfer of strain across the interface. This step is shown in Figure 21 (a).

v. The bonding agent is left to cure for 24 hours. The tape and binding clip are removed. The fully cured FBG-Diaphragm component is seen in Figure 21 (b).

vi. The FC/APC Connector of the fibre is connected to a light source and/or optical interrogator to ensure that a signal is produced and to confirm the default centre wavelength. Upon completing this check, the sensor is now prepared to be fixed in the housing.

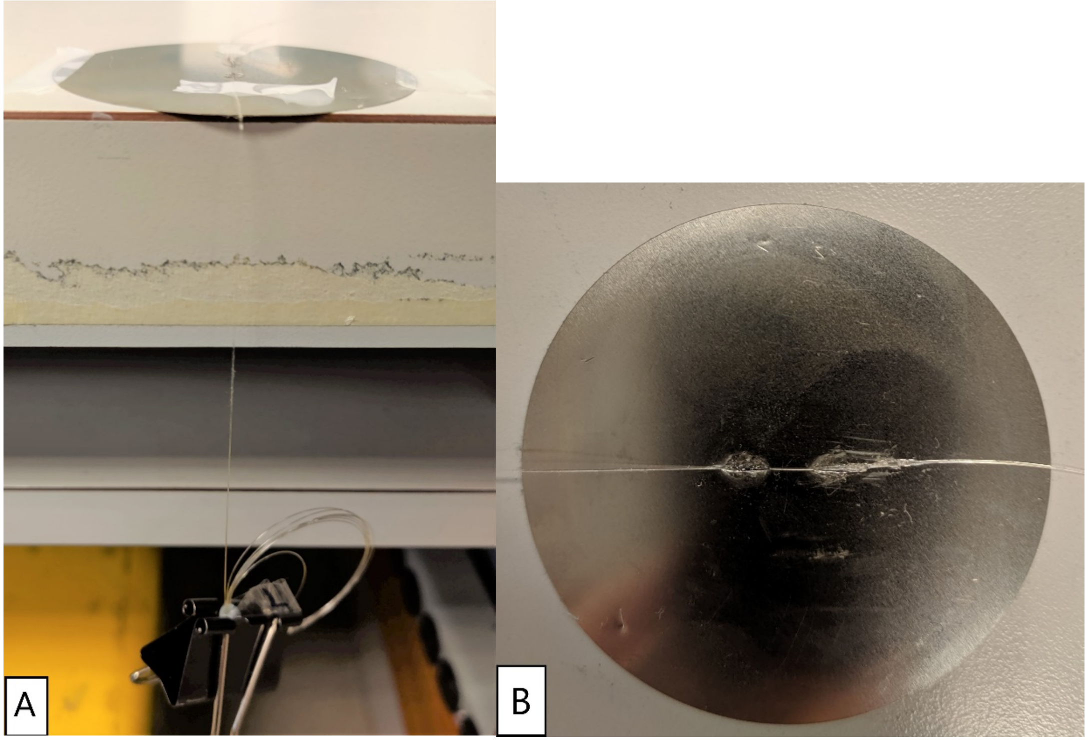

Figure 21: A fibre with an embedded FBG in the bonding process with a diaphragm (a). A completely cured FBG-diaphragm (b).

4.2 Test rig designs

The following sections will present the drawings and descriptions of the test rigs for atmospheric and target depth pressure testing. The testing procedure for each rig is discussed with the results shown in Chapter 5.

4.2.1 Atmospheric pressure rig

The purpose of the first design is to validate the use of Equation 2.4 which gives strain at the centre of rigidly fixed diaphragm based on constant physical parameters and a varying pressure load. The applied pressure is relative to atmospheric pressure and so the structure is designed to accommodate this condition.

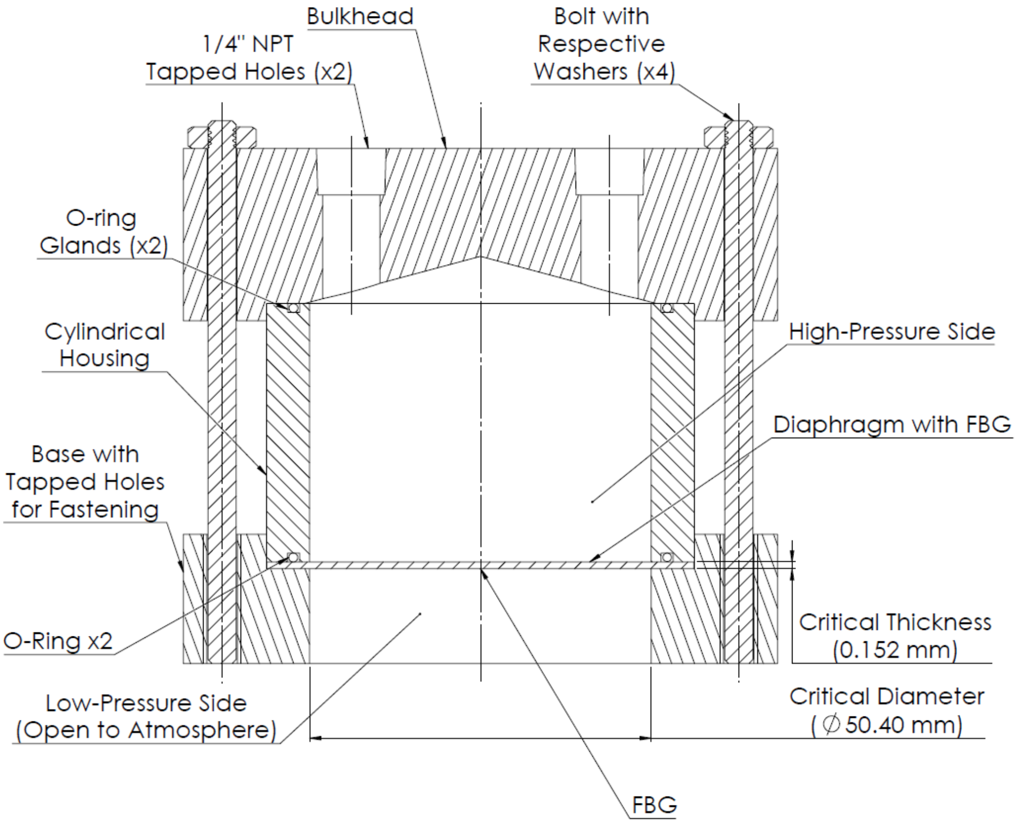

Figure 22: Atmospheric test rig design. FBG not shown, label indicates where the FBG is placed.

The schematic in Figure 22 depicts the basic assembly including the diaphragm fixed between the edge of the base and cylinder. As labelled, one side is exposed to the atmosphere (low-pressure side) while the other has pressure supplied by a screw pump (high-pressure side) to simulate a change in water column height. The full experimental configuration is displayed in Figure 23.

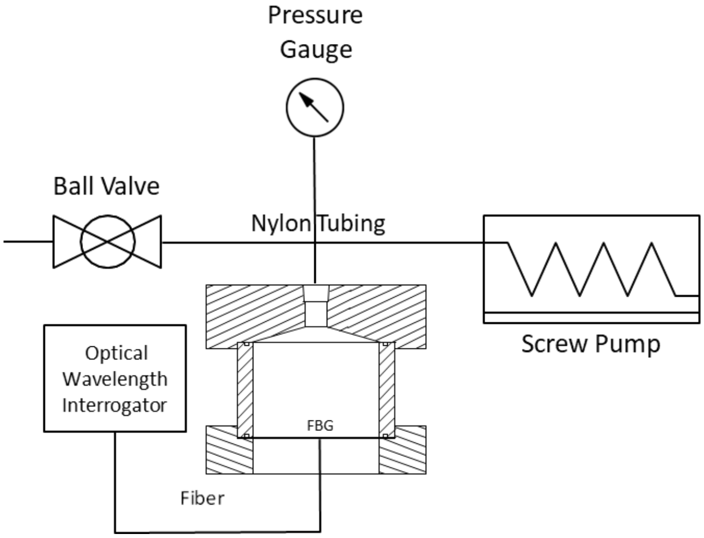

Figure 23: Configuration Schematic for Atmospheric Testing

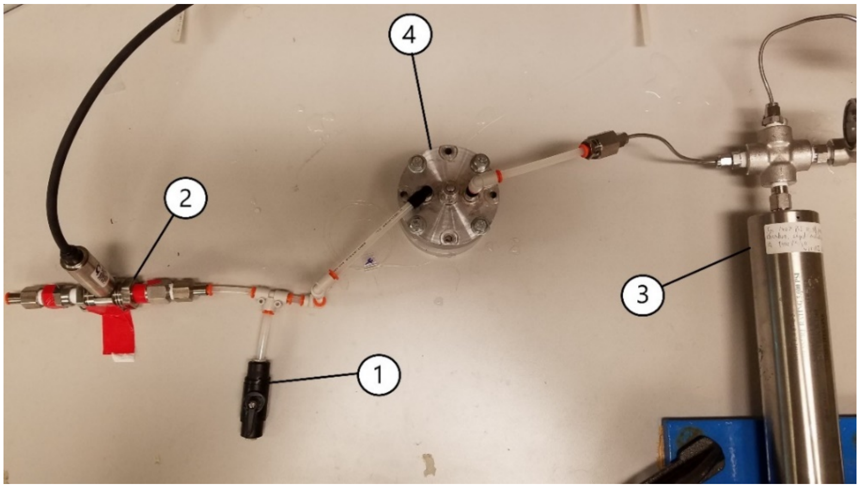

Figure 24: Lab bench setup for atmospheric testing. Ball valve (1), pressure Gauge (2), screw pump (3), and sensor (4). FBG and optical wavelength interrogator are not shown in this figure.

The following procedure was used in preparation for testing and gathering readings during testing:

i. The screw pump is primed by drawing water into its chamber and then purging any remaining air out of the system as best as possible. The sensor housing with a mounted FBG-Diaphragm is fastened with bolts that feed into a threaded base. The bolts are torqued to 0.2 Nm to provide an O-ring seal. This allows minimal clamping force on the diaphragm, thereby reducing the possibility of altering the mechanical behaviour of the diaphragm.

ii. The nylon tubing is fit together with the components shown in Figure 24 using push-to-connects. Water is forced through the system by turning the screw pump handle, thereby replacing air which is expelled through the opened valve.

iii. To gather measurements, the screw pump is turned to decrease the volume of the system thus driving up the pressure. The pressure transducer is used as a reference sensor to determine the pressure applied, shown as a voltage. When the equivalent of approximately 1 cm of H_2O pressure is applied, an increment of pressure is recorded making note of the voltage output by the pressure gauge and the wavelength peak determined by the interrogator. This is process is continued until a chosen number of recordings are made.

4.2.2 Differential pressure rig

Whereas the sensor presented in Section 4.2.1 was designed to confirm the fundamental mechanical description of the diaphragm, this second iteration of the design phase more closely emulates the sensor design described in Chapter 3. Since the pressurization mechanics differ and the piston is omitted, this experimental design can be implemented in a lab bench setting. The pressures adopted for testing are safe for basic laboratory conditions and represent values typical for shallow coastal waters. The schematic for this design is shown in Figure 25.

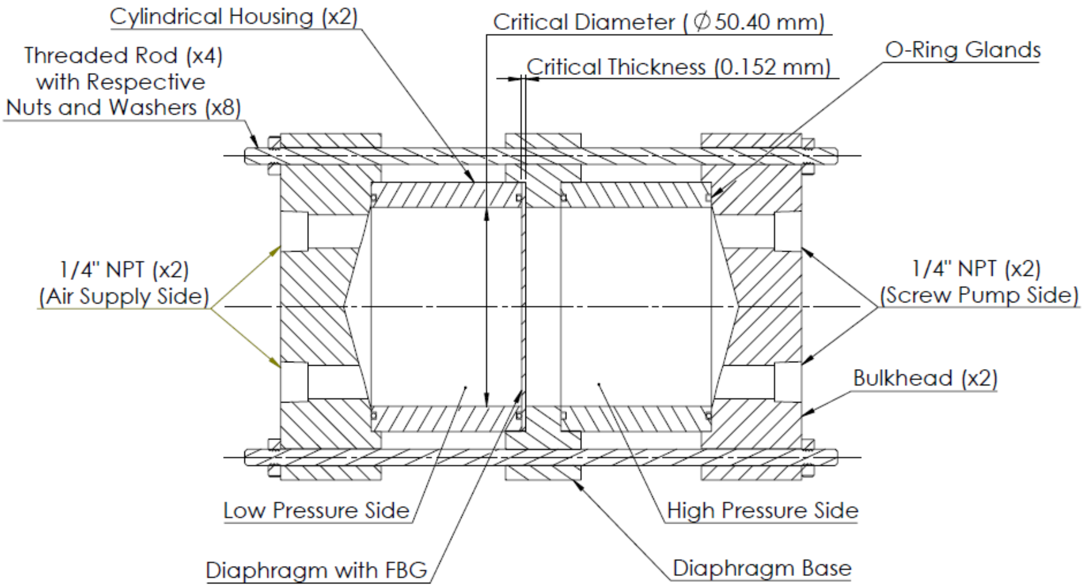

Figure 25: Differential pressure test rig design. Diaphragm thickness is not to scale with the rest of the design.

In this instance, the diaphragm is fixed between two spaces of definite volumes containing two fluids, the high-side and low-side as seen in Figure 25. With a highly compressible fluid on the low-side and relatively incompressible fluid on the high-side (air and water for testing purposes respectively), the diaphragm will deflect in the presence of a differential pressure between the two sides. To achieve a differential pressure at a target depth pressure above atmospheric pressure the experimental configuration shown in Figure 26 is utilized.

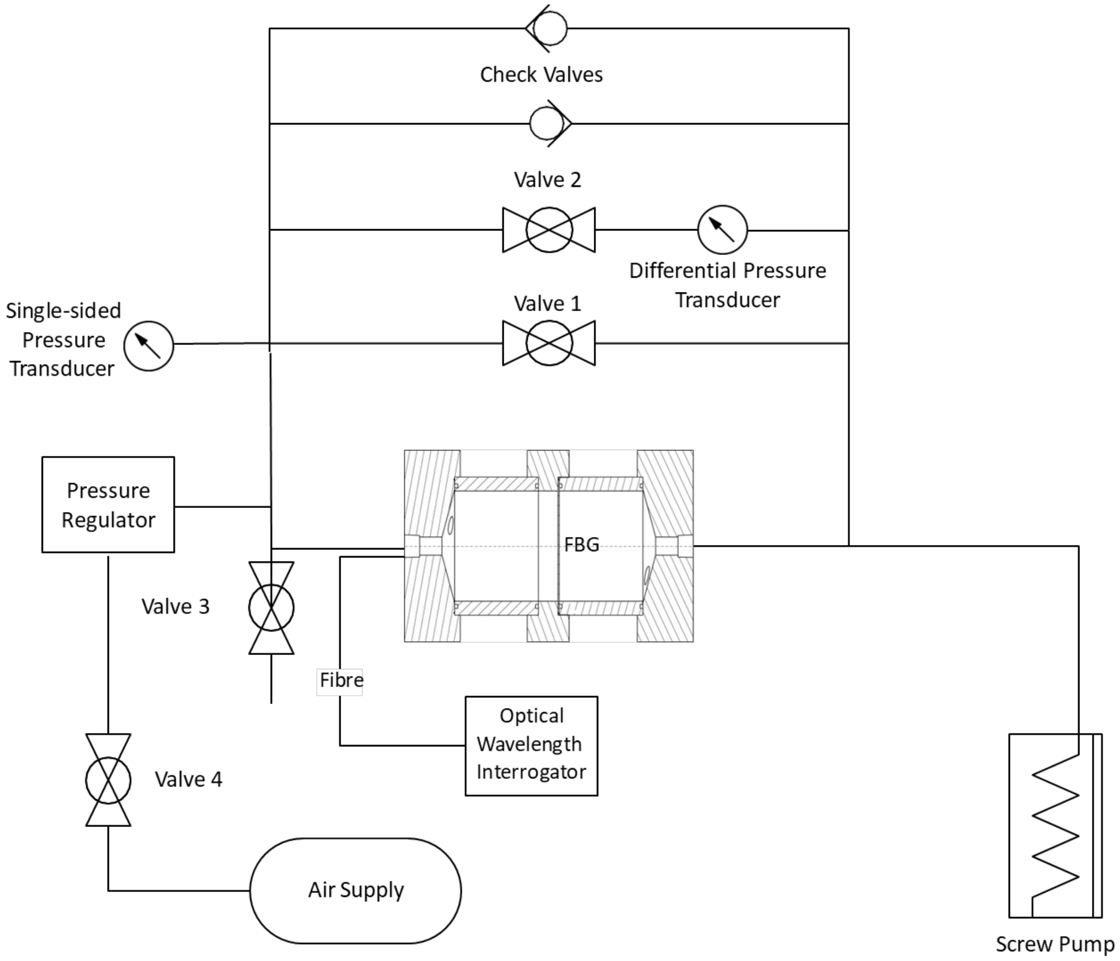

Figure 26: Experimental configuration for differential pressure testing. Two check valves serve as a precautionary measure to equilibrate the pressure from either side in case of pressure differential that exceeds the rated pressure of the transducer.

The configuration is designed in a manner that would ensure the diaphragm stays structurally intact through the use of a set of check valves and on/off valves seen in Figure 26. The check valves function in the case of a pressure surge occurring on either side whereas the on/off valves maintain isolation and between the two sides of the systems and the differential reference sensor. The air supply seen in Figure 26 is used as a reservoir to facilitate a target depth pressure, P_{ext}, of the system while the pressure regulator is used to set this pressure. The screw pump is the device that is meant to provide an incremental pressure change, ΔP_{ext}, causing a differential pressure in the system once the target depth pressure is assumed. The associated changes in strain due to ΔP_{ext} are then interpreted by the FBG and interrogator. The actual experimental configuration is displayed in Figure 27.

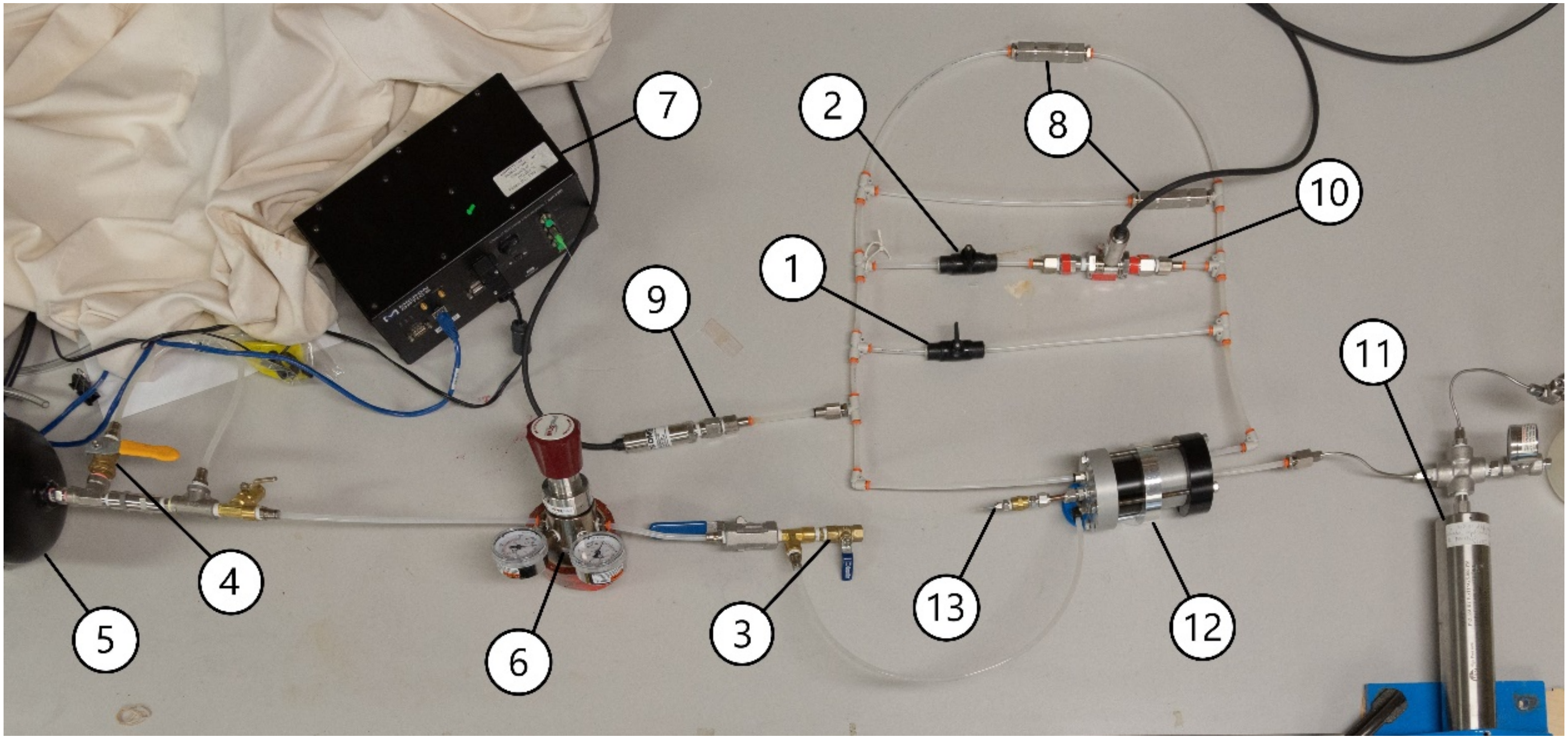

Figure 27: Actual experimental configuration for differential pressure sensor. (1) Valve 1, (2) Valve 2, (3) Valve 3, (4) Valve 4, (5) Pressurized Air Tank, (6) Pressure Regulator, (7) Optical Wavelength Interrogator, (8) Check Valves, (9) Single-sided Pressure Transducer, (10) Differential Pressure Transducer, (11) Screw Pump, (12) Sensor, (13) FBG Feedthrough

The following testing procedure is adopted for this design configuration:

a. The system is primed with water and valves are positioned to allow both sides of the sensor to be in connection. The target depth pressure is set with the regulator at 10, 20, 40, and 60 psi (7, 14, 28, and 42 mH_2O) with a set of trials being done at each pressure.

b. The handle of the screw pump is manually turned incrementally to create a set of detectable pressure changes (ΔP_{ext}) in the system. The pressure reading is cross-referenced with the wavelength peak determined by the optical interrogator and is recorded.

c. The screw pump is turned back to return to approximately the original system pressure and the on/off valves are reopened thereby re-equilibrating the system pressure. Results at different system pressures are compiled by repeating these steps.

The results produced with this through the testing of this configuration is seen in Chapter 5.

4.3 Finite element analysis formulation

A Finite Element Analysis (FEA) is conducted for an FBG-diaphragm structure to gain an understanding of whether a bonded fibre with a diameter comparable to the thickness of the diaphragm can alter the mechanical behaviour of deflection. Conducting an FEA involves multiple steps to create the model and form the mesh. This section outlines the process taken to create an FEA model that represents the FBG-Diaphragm structure.

The model of the optical fibre and diaphragm was developed using Siemens NX 9.0. Only one-quarter of the diaphragm is modeled, as shown in Figure 28 (a), taking advantage of symmetry. The fibre is modeled as one-quarter of its full geometry, as shown in Figure 28 (b) and (c), in semicircle-rectangle shape. The adhesive to instrument the fibre to the diaphragm is not included in the analysis as the bond is formed on the end of the fibre and therefore does not come in contact with the centre the fibre (see Figure 20).

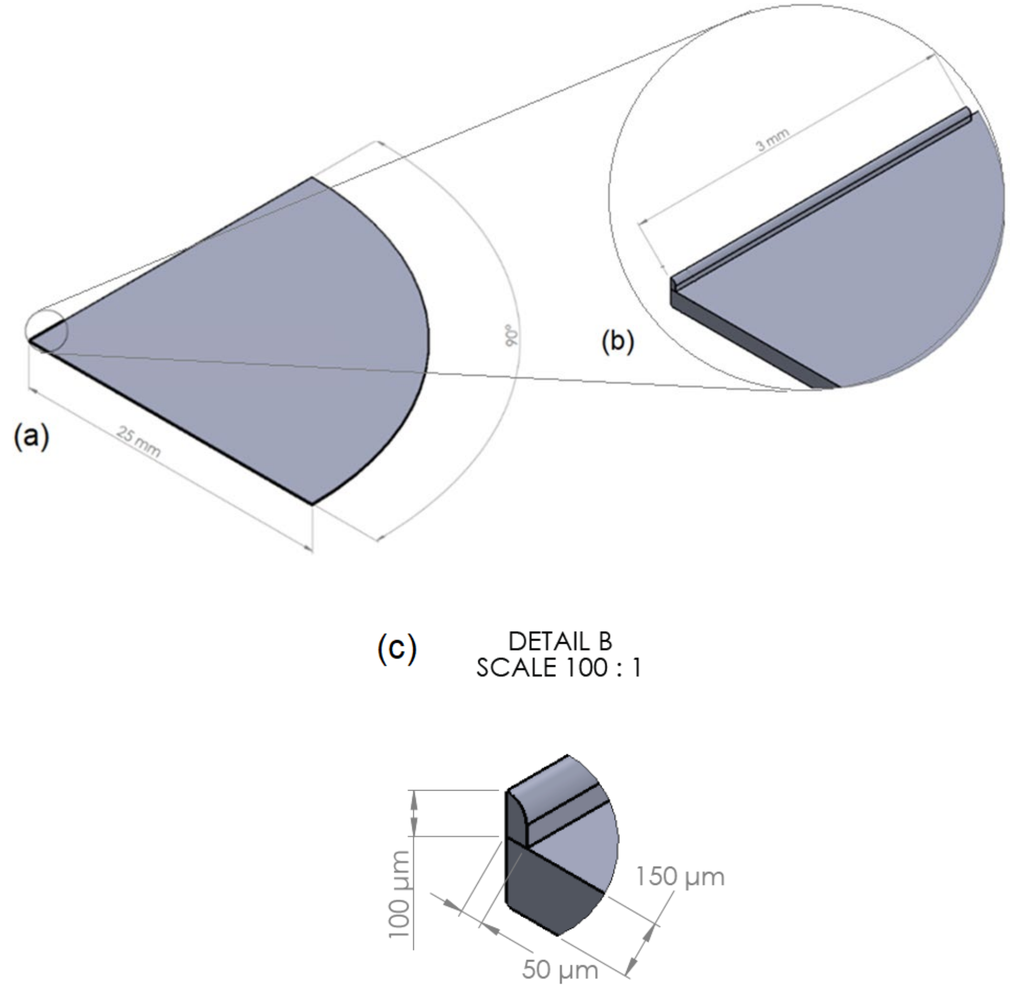

Figure 28: Diaphragm Wedge Assembly Model Geometry with Dimensions. In (a), a quarter wedge of a diaphragm is shown with an FBG. In (b), a close up of the FBG is shown demonstrate the length. In (c), A close up of the cross-sectional geometry of a the FBG is shown.

With the assembly geometry defined, a three-dimensional mesh with CTETRA(10) solid element type is inferred by the software based on the mesh control applied at the points of interest. The mesh control is done so by selecting the faces of the model that require a high precision, namely on the fibre and inner cross-sectional faces of the diaphragm wedge. A mesh size of 0.01 mm is controlled along these notable sections, whereas the mesh for the rest of the model is inferred. The mesh employed is seen in Figure 29 and Figure 30.

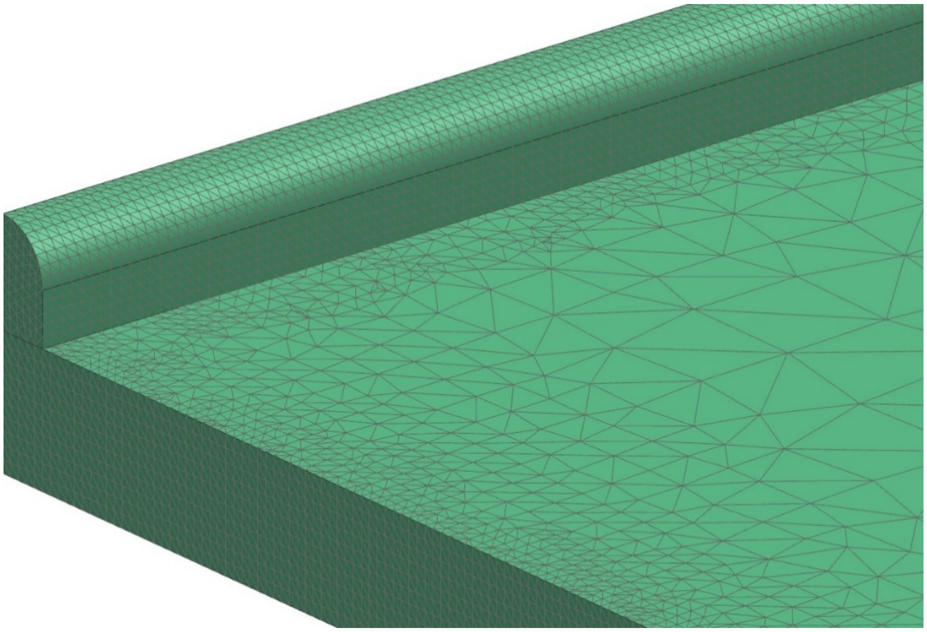

Figure 29: Isometric view of FBG-diaphragm wedge meshing.

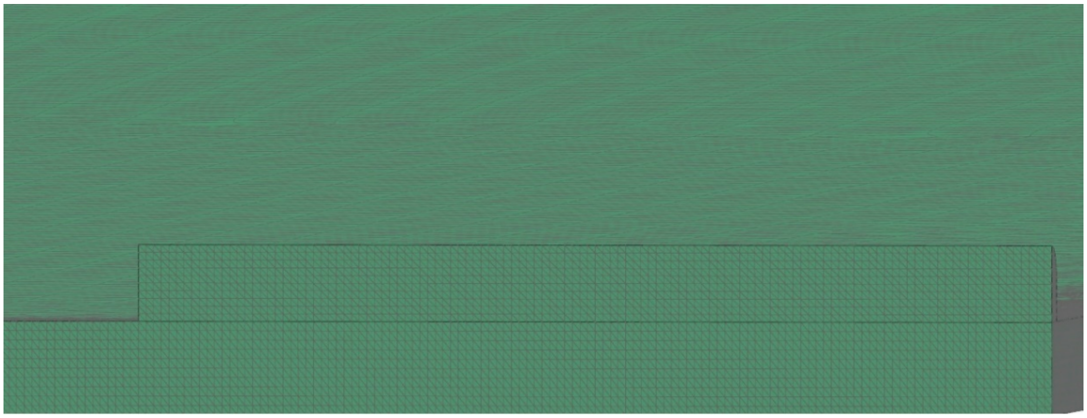

Figure 30: Front view of FBG-diaphragm wedge meshing.

A mesh refinement study was executed to ensure that the mesh size selected is consistent with results found with other mesh sizes. The tested controlled mesh sizes varied from 0.05mm to 0.01mm with each run observed for major discrepancies in strain output. The study revealed that once the mesh size controlled for was smaller than 0.04mm, the strain at the centre was within 0.05% for subsequent sizes. A controlled mesh size of 0.01mm was selected to ensure that the nodes on the FBG and diaphragm would be in alignment.

Following the meshing, the material properties are set. A pressure load of 98 Pa or 1 cmH_2O is applied to the underside of the diaphragm. A 6-DOF fixed constraint is applied to the outer periphery of the wedge. A symmetry constraint is applied to the flat perpendicular cross-sectional faces of the diaphragm wedge and fibre to allow the behaviours on both sides to be mirrored. Lastly, the simulation object type is determined, where surface-to-surface gluing is used to completely bond the nodes on bottom surface of the fibre to the nodes on the top surface of the diaphragm.

NX 9.0 deploys Nastran as the solving software which creates a simulation and mesh file based on user-defined parameters. In this analysis, a default structural simulation setup is selected, and a strain output option is designated in addition to stress and displacement. The software solves the mass matrix generated based on the input specifications for the model. The model runs with an external convergence criterion of AREX which takes the residual vector of the current iteration and divides it by the initial load vector. The convergence tolerance is taken as 1E-08 and is computed in approximately 800 iterations. The results of the FEA model are presented in Chapter 5.

Chapter 5 - Results and discussion

5.0 Introduction

A series of experiments was performed using the various test methods described in Chapter 4 to verify the performance of the sensor design model. The following sections outline and discuss the results acquired from the test sensors and the FEA findings. In the two design configurations, experimental sensitivity is determined and compared to theoretical sensitivity. The experimental sensitivity is determined as the slope of Bragg wavelength in response to pressure. Furthermore, the pressure relationship between the two sides of the diaphragm in differential pressure design is examined.

5.1 FEA results

A set of FEA solutions was generated based on the procedure outlined in Section 4.3 to gain an understanding of the behaviour in the diaphragm-FBG structure that goes beyond basic theoretical modeling. Three critical behaviours are examined in the analysis: i) the effect of a varying fibre modulus on strain, ii) the strain profile from the top of the fibre to the bottom of the diaphragm, and iii) the strain profile at the centre of the fibre. Strain is computed and compared to calculations produced by the model developed in Chapter 3. The FBG sensitivity to strain is a constant factor (1.2 pm/με) determined from Equation (2.7).

The first consideration is the possible influence of a bonded fibre on the effective stiffness of a diaphragm. The principal concern here is that a fibre of similar diameter to the diaphragm thickness could produce an unintended reinforcing effect on the diaphragm that might cause a deviation from the predicted theoretical sensitivity.

The FEA model was solved for a series of fibre moduli (E_{fibre}) and an applied pressure (ΔP_{ext}) of 1 cmH$_2$O (98 Pa), producing a set of results describing the strain in the diaphragm that corresponds to the axial coordinate in the fibre (ε_{yy}). The model was first computed without a fibre, producing an ε_c ($5\ \mu\varepsilon$) that matches the tabulated strain using Equation (2.5). The strain ratio is determined as the difference between the strain with a varying fibre modulus versus the strain without a bonded fibre ($\varepsilon_c\left(E_{fibre}\right)\!:5$). These findings have been compiled into Figure 31.

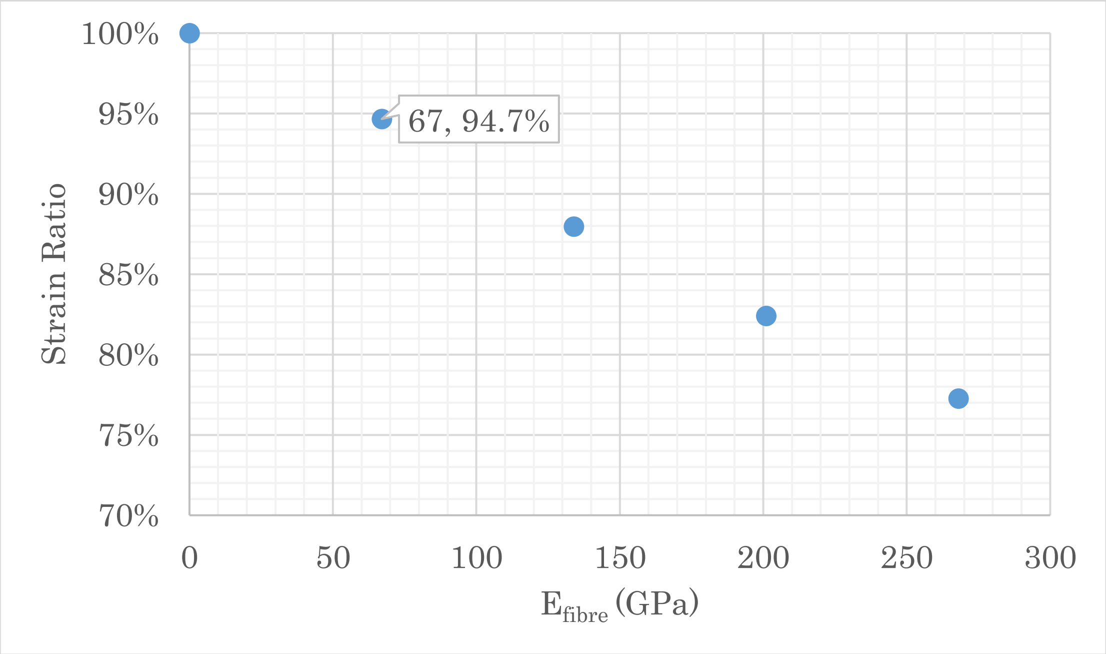

Figure 31: Strain ratio of diaphragm-FBG model versus varying fibre moduli. The ratio is with respect to the strain in diaphragm without a bonded fibre. The fibre modulus employed in the experimental design is called out in the plot.

As is clear from the figure, the strain ratio decreases as E_{fibre} increases. This behaviour is to be expected since the diaphragm deflects less due to the increasing reinforcement of stiffer fibres. The actual E_{fibre} within the design (67 GPA, see Table 3) would impart only a 5% drop in strain output and thus an equivalent drop in sensitivity. Consequently, FBG should not significantly disrupt the inherent behaviour of the diaphragm.

The FEA model also provides insight into the strain profile of the structure. The FBG-diaphragm wedge is examined on the inner face and a strain gradient diagram is displayed in Figure 32.

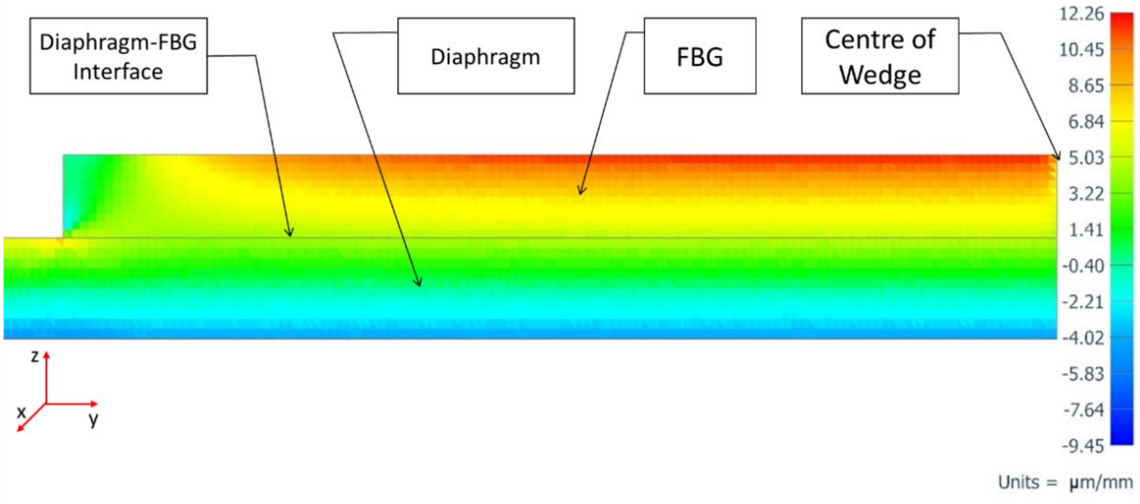

Figure 32: YY strain gradient across longitudinal face of FBG and diaphragm.

The strain gradient profile behaves as expected: the neutral axis of the structure (plotted in teal green) is found at the midplane of the diaphragm and the FBG produces only positive strain if the furthest edge from the centre is disregarded.

The strain profile proceeding from the top of the fibre to the bottom of the diaphragm at the centre of the wedge is shown in Figure 33.

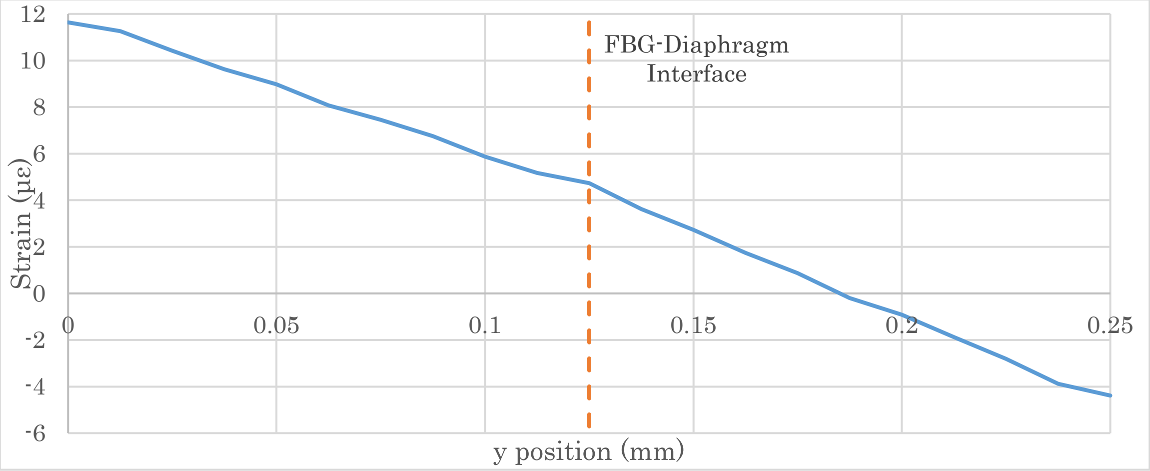

Figure 33: Strain from the top of fibre to bottom of diaphragm.

The strain is observed to decrease in a linear fashion, with the material transition at the interface of the FBG-diaphragm wedge negligibly affecting the strain profile. Strain at the interface is 4.73 με and the neutral axis of the diaphragm is noted to lie at a position of approximately 0.186 mm.

The strain observed from the centre of the FBG to the outer mounting point stays relatively consistent until approximately the last tenth of the FBG's length. A strain profile from the centre of the FBG is displayed in Figure 34.

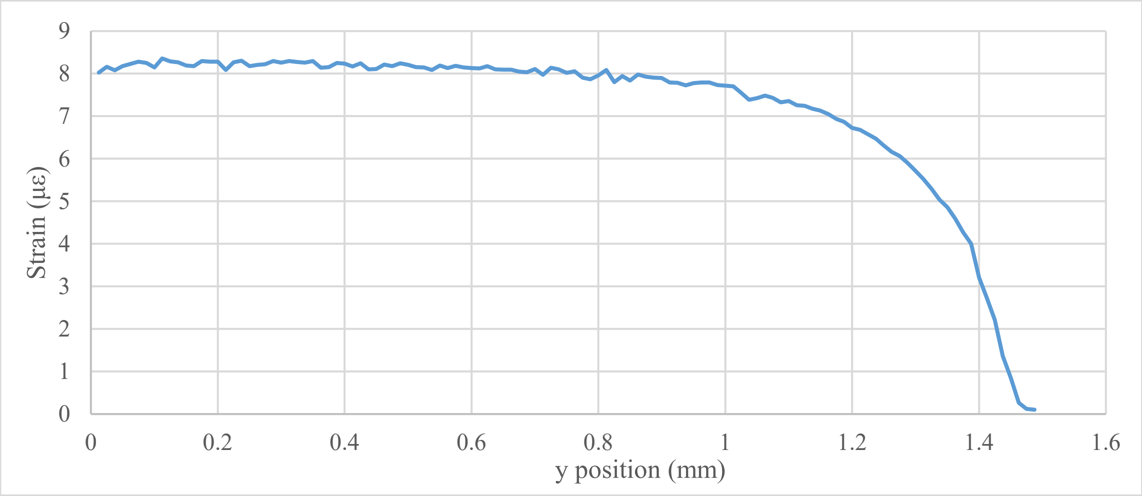

Figure 34: Strain along the central axis of the fibre starting at centre of the wedge.

The observed strain is approximately 8 με/cmH_2O for half of the fibre starting at the centre of the wedge structure (0 to 0.75 mm). After 1.1 mm of length, the strain sharply drops to nearly 0 at a length of 1.5 mm. Numerically this can be described as occurring along the last 26% of the fibre length. When considering a fibre length of 3mm (twice the length), the same phenomenon occurred at approximately the last 22% of the way along the fibre. This occurrence suggests that the FBG should reside in the flat region of the plot to avoid nonlinear behaviour. Therefore, the length of fibre optic core that is bonded to the diaphragm should be long relative to the overall grating length of the FBG.

5.2 Single-sided sensor design for atmospheric operating pressure

The testing for this design is the simplest in terms of experimental setup, hardware requirements, and procedure. Thus, it was the starting point for the experimental work and provided a basic understanding of the behaviour of FBG-diaphragm sensors. The experiments employing the sensor design described in Section 4.2.1, were conducted in four trials. The results for Trial 1 are shown in Figure 35. The scatter plots for the other trials share a similar profile and are not shown.

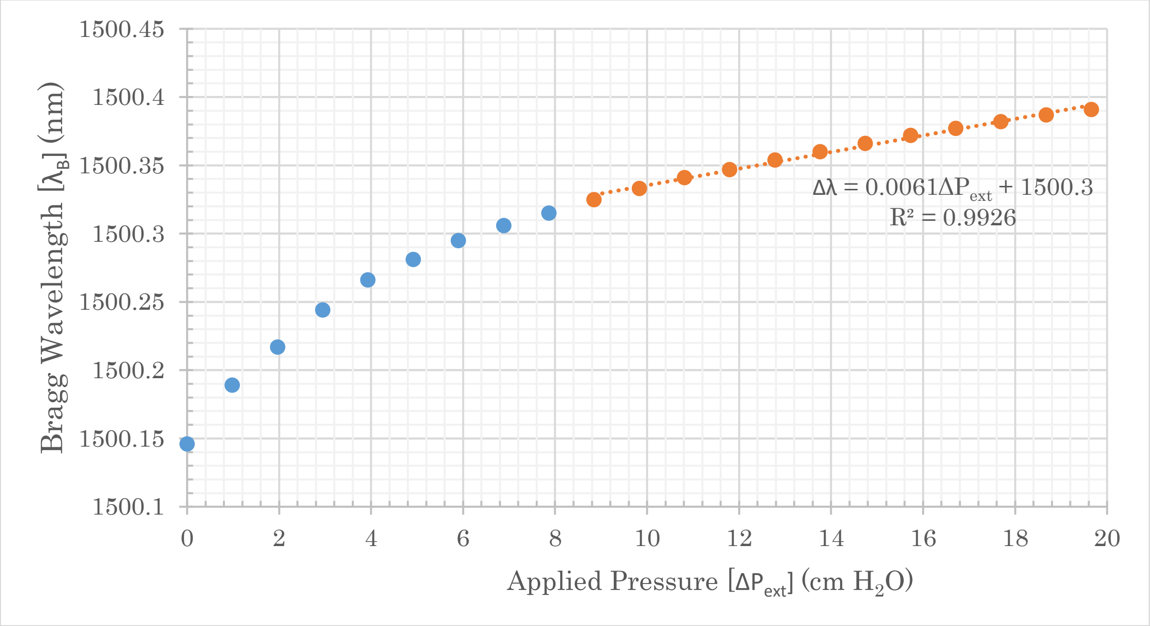

Figure 35: Experimental results at atmospheric pressure for Trial 1. The scatter profiles for the other trials are similar and are not shown. The increment between data points was selected based on the closest discernible output from the pressure transducer according to 0.014 psi=0.982 cmH_2O.

The sensitivities and coefficients of determination for each trial are presented in Table 3.

Table 3: Experimental results across four trials. The coefficient of determination is R^2.

	Sensitivity (pm/cmH_2O)	R^2
Trial 1	6.10	0.993
Trial 2	6.40	0.987
Trial 3	5.90	0.980
Trial 4	5.80	0.992
Mean	6.05	-
Theoretical	6	-

As shown in Figure 35, the Bragg wavelength increases in response to an increase to ΔP_{ext}. There are two components to the relation evident in the data: one which is distinctly non-linear (in blue) and a second which exhibits a near-linear profile (in orange). Only the second component of the data set is considered in computing sensitivity, as rationalized in further detail in the Discussion. The calculated sensitivities across the four trials conducted were 6.1 pm/cmH_2O, 6.4 pm/cmH_2O, 5.9 pm/cmH_2O, and 5.8 pm/cmH_2O; all with a coefficient of determination (R^2) above 0.98 which suggests a strong linear relation.

The theoretical sensitivity of the diaphragm was determined to be 6 pm/cmH_2O at an atmospheric operating pressure (refer to Figure 19). The mean of the experimental sensitivities is 6.05 pm/cmH_2O and all of the trials were within 5.8% of the value predicted by theory. The mean sensitivity is 0.83% different from the theoretical value. Consequently, the fabricated sensor appears to honour the essential elements in the model design.

5.3 Differential pressure sensor design

Two similar types of experiments were conducted using the differential pressure sensor design developed in Section 4.2.2. One describes the experimental sensitivities at various target depth pressures whereas the other compares the observed pressure ratio for pressures on either side of the diaphragm face. The format of the experiments consisted of conducting three trials at four overall target depth pressures (ΔP_{ext}): 10, 20, 40, and 60 psi (7, 14, 28, and 42 mH_2O).

5.3.1 Pressure ratio test

An experiment which examines the pressure input-output response of both sides of the diaphragm was performed. This experiment requires that pressure measurements be taken from both sides of the diaphragm and plotted against each other for comparison with theoretical predictions. Figure 36 depicts the observed pressure ratio for a target depth pressure of 10 psi (7 mH_2O) which resembles the behaviour observed at higher target depth pressures. There are two sides of a deflecting diaphragm, the high-pressure side and low-pressure side. The high-pressure side represents ΔP_{ext} and is controllable by the screw pump which generates an applied pressure to cause the diaphragm to deflect. The Low-Pressure Side represents ΔP_a and is the opposing side which reacts with a resultant pressure increase due the surrounding volume reduction caused by the diaphragm deflection.

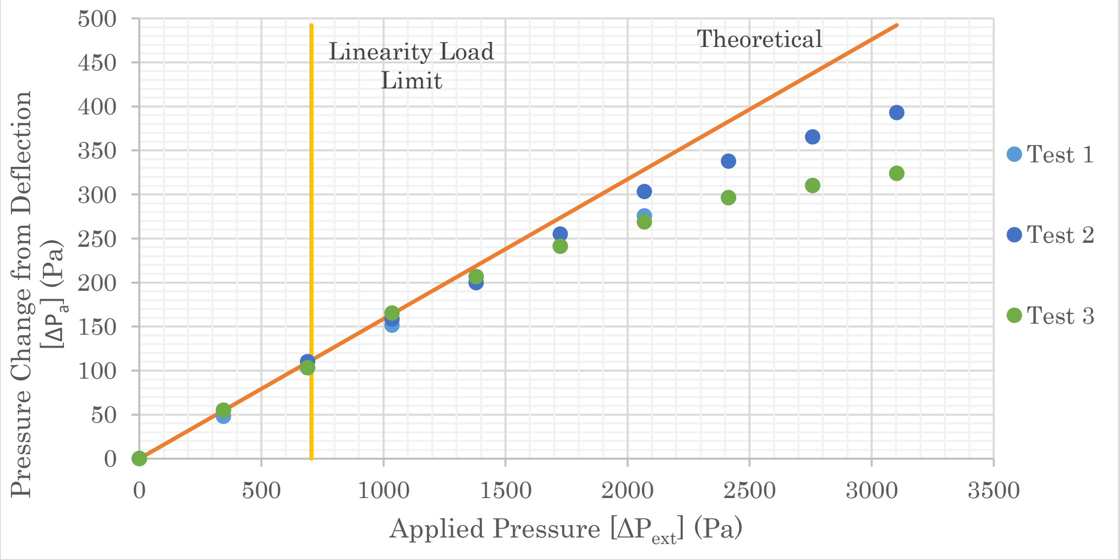

Figure 36: Pressure ratio at 10 psi target depth pressure.

As ΔP_{ext} increases, ΔP_a grows linearly within the predicted linear range [0-750 Pa] and several increments thereafter. Beyond 1500 Pa, nonlinearity is observed which causes the experimental curve to deviate below the theoretical curve. This phenomenon is noted across all target depth pressure experiments as documented in Table 4 and Table 5.

Table 4: Pressure response ratios across a set of trials and Target Depth pressures.

Target Depth Pressure (psi)		Pressure Ratio Slope	R^2
10	Trial 1	0.148	0.9993
	Trial 2	0.154	0.9990
	Trial 3	0.158	0.9978
	Mean	0.153	
20	Trial 1	0.212	0.9979
	Trial 2	0.200	0.9920
	Trial 3	0.198	0.9945
	Mean	0.203	

40	Trial 1	0.304	0.9976
	Trial 2	0.298	0.9994
	Trial 3	0.296	0.9984
	Mean	0.299	
60	Trial 1	0.358	0.9997
	Trial 2	0.354	0.9960
	Trial 3	0.352	0.9992
	Mean	0.355	

Table 5: Comparison table of mean experimental and theoretical pressure ratio slopes

Pressure Ratio Slope			
Target Depth Pressure (psi)	Mean	Theoretical	% Difference
10	0.153	0.159	3.38%
20	0.203	0.209	2.90%
40	0.299	0.295	1.61%
60	0.355	0.363	2.35%

The mean of the pressure ratio slope is determined at each tested target depth pressure and compared against the theoretical slope in Table 5. The differences between the two are under 4% with the target depth pressure at 40 psi showing the least difference at 1.61%.

5.3.2 Experimental sensitivity

The next step taken was to characterize the sensitivity achieved in the differential pressure design. In doing so, the experimental configuration displayed in Figure 26 is adopted and the procedure described in Section 4.2.2 is carried out. The experimental results are displayed in plots that compare sensitivity in response to applied pressure. Figure 37 demonstrates the observed profile plot at 10 psi target depth pressure, which is representative across all other target depth pressures.

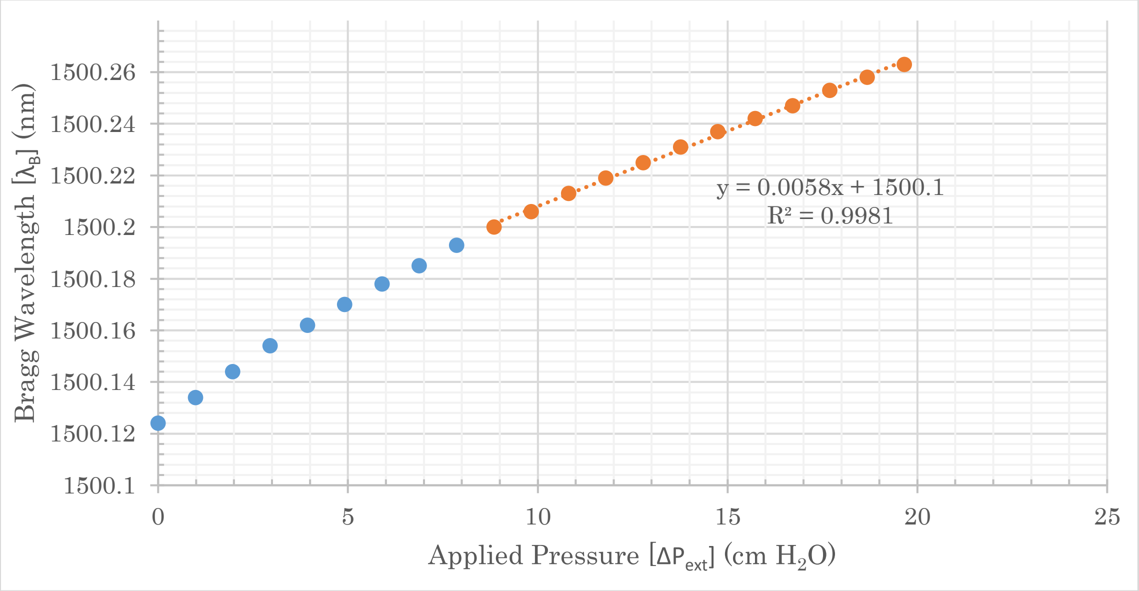

Figure 37: Differential pressure sensor experimental sensitivity at 10 psi target depth pressure.

Table 6: Experimental sensitivities across a set trials and target depth pressures.

Target depth pressure (psi)		Sensitivity (pm/cmH2O)	R^2
10	Trial 1	5.80	0.9981
	Trial 2	5.60	0.9971
	Trial 3	5.50	0.9977
	Mean	5.63	-
20	Trial 1	5.70	0.9978
	Trial 2	5.80	0.9963
	Trial 3	5.80	0.997
	Mean	5.77	-
40	Trial 1	5.70	0.9985
	Trial 2	5.60	0.9985
	Trial 3	5.80	0.998
	Mean	5.70	-
60	Trial 1	5.70	0.9989
	Trial 2	5.70	0.9984
	Trial 3	5.60	0.9978
	Mean	5.67	-

Table 7: Comparison of mean and theoretical sensitivities for their respective tested operating pressures.

	Sensitivity (pm/cmH2O)		
Target depth pressure (psi)	Mean	Theoretical	% Difference
10	5.63	5.98	5.8%
20	5.77	5.93	2.8%
40	5.70	5.74	0.7%
60	5.67	5.45	4.0%

The sensitivity for the data in Figure 37 is determined in the same manner as for those in Figure 35. The experimental sensitivities for each trial in Table 6 all indicate a strong coefficient of determination. The mean sensitivity across the three trials at each target depth pressure is determined and compared to the theoretical sensitivity in Table 7. The percent error among all target depth pressures is below 6%, with a mean sensitivity at target depth pressure of 40 psi which most closely approaches the theoretical sensitivity out of all tested target depth pressures.

5.4 Clamping torque examination

A point of concern was the potential effect that clamping the diaphragm has on sensitivity and its profile. To investigate this issue, the procedure outlined in Section 4.2.1 is used and the overall sensitivity is compared to the torque applied to the sensor housing for that test. The torques tested are 0.23, 0.57 and 1.13 Nm, and results are shown in three plots displayed in Figure 38.

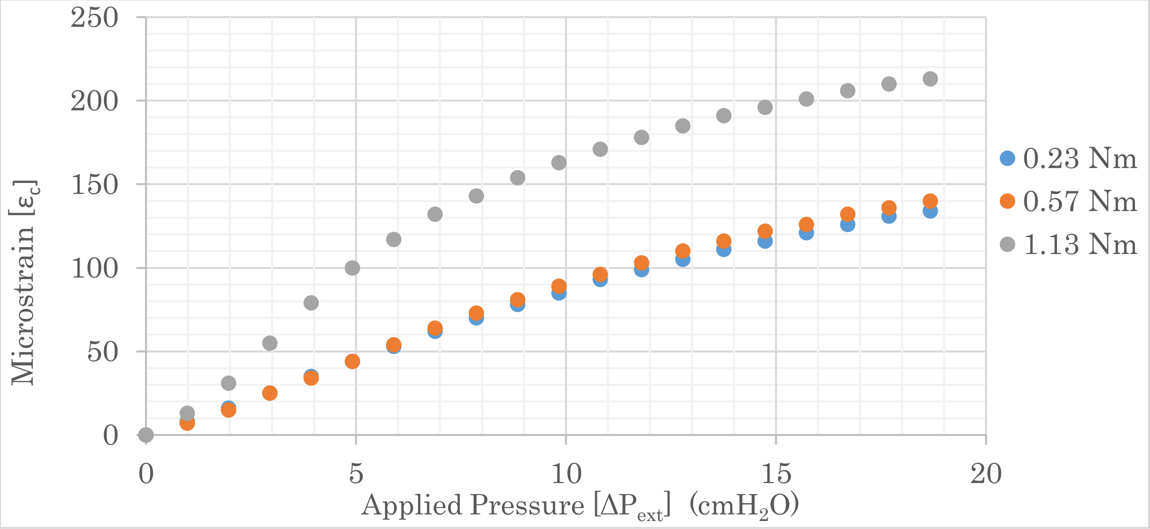

Figure 38: Pressure response at various clamping torques. A strain-gauge-based diaphragm transducer was used in these testing instances and thus the output is displayed directly in microstrain.

This figure indicates that a sensor fixture with fasteners torqued at 1.13 Nm, the highest torque tested, produced a response that has the most pronounced curvature (i.e. non-linearity) and highest sensitivity among the torques tested. The tests conducted at 0.57 and 0.23 Nm had a more linear character where the trial at 0.57 Nm had a slightly higher sensitivity than the trial at 0.23 Nm. This would suggest the amount torque applied to fasten and seal the sensor housing changes the behaviour of the diaphragm such that a higher torque increases sensitivity and increases the curvature of the plot profile. However, a more intensive analysis would be required to better understand and quantify this phenomenon.

5.5 Discussion

The FEA findings validate the theoretically developed model of an FBG-diaphragm structure. The results of the FEA indicate that an FBG core does not significantly reinforce the diaphragm. The difference in Young’s modulus of the germanosilicate fibre core and the diaphragm negates any significant interference caused by the core with respect to strain in the diaphragm despite the similarity between the diaphragm thickness and FBG diameter. From Figure 34, the strain observed along the central axis of the FBG would nosedive to nearly zero along the last quarter of the fibre length away from the centre which can contribute to the nonlinear response and inaccuracies observed in the findings from experimental testing. Whether this is to be trusted and how this phenomenon occurs in a practical sense requires a more comprehensive experimental examination.

The testing procedure at atmospheric testing conditions with the single-sided sensor yielded the results displayed in Figure 35 and Table 3. In considering the sensitivities for both sensor designs at each trial, an initial amount of pressure was omitted to allow the diaphragm to be worked in.

With regards to the differential sensor design, the experimental sensitivity plot profile differed slightly from the single-sided pressure testing. This difference is primarily the prominence of the curve in the initial data set of the curve, which appears to be less pronounced than the corresponding data set considered for the single-sided sensor configuration (see Figure 35 and Figure 37). This could be due to the presence of an applied pressure exerted to both faces of the diaphragm, that might partially nullify imperfections as a result. The slopes of the two data sets for this differential sensor design are also more numerically similar to each other than in the single-sided sensor configuration.

When comparing Table 5 and Table 7, (i.e. outcomes of pressure ratio and experimental sensitivity testing for differential sensor design respectively), the best performance occurred at an target depth pressure of 40 psi. Conversely, the largest percent difference between mean and theoretical values was observed at 10 psi in both cases. This may be a coincidence, but further examination is necessary to confirm whether this is a consistent effect.

It was observed throughout the experimental trials with various diaphragm configurations (especially with the single-sided sensor configuration) that an initial base amount of pressure was necessary to stress the diaphragm into a state that allows linear behaviour to develop. It is possible that the small diaphragm thickness could be amplifying the influence of inherent geometric imperfections. The diaphragm manufacture may have introduced imperfections and deviations from the idealized geometry. Thus, by exposing a baseload of pressure, it is possible that such imperfections could be mitigated as increasing pressure is exerted across the face.

Another possible reason for this behaviour may lie in the fixing and sealing method of the sensor. A handbook available by Vishay Precision Group on Design Considerations for Diaphragm Pressure Transducers suggests that a diaphragm and its fixture should be constructed as a homogenous unit to ensure maximum accuracy [29]. A diaphragm with a homogenous fixture was manufactured, however given the small thickness required, the outcome of this was a diaphragm with notable geometric imperfections that ultimately yielded consistent and accurate performance. To construct a stainless-steel diaphragm with a thickness of 0.15 mm, using shim stock was the only feasible solution given the available facilities and resources. Utilizing shim stock with anisotropic geometric properties will introduce another source of error.

When assembling the sensor, the seal is formed pressing an O-ring against a diaphragm resting on its base. This fixture mode and its potential to introduce variations in a diaphragm behaviour, has been examined in Section 5.4. Figure 38 indicates that the greatest non-linear plot profile occurs at a fastening torque of 1.13 Nm, the highest torque tested. This data set also shows the greatest sensitivity relative to the other tested torques. This suggests that any amount of torque may increase deflection and thus sensitivity.

The process of bonding an FBG to a diaphragm is likely an additional source of error in the observed sensor response. The state of the FBG immediately before the adhesive settles to form the static bond could potentially alter its initial response to strain. Dispersion of the adhesive may not be evenly distributed.

Furthermore, given FBGs sensitivity to changes as small as 1 microstrain, the tension introduced by the suspended paper binder during the bonding process could possibly overextend the FBG such that it is in a pretensioned state even if the diaphragm is unstressed. This may present errors in the response to pressure as strain is transduced from the diaphragm to FBG. In hindsight, a range of paper binder sizes could have been trialled to assess a possible dependence. The process of bonding is likely the greatest source of error for the study given the difficulty in achieving reproducible results. Overall, bonding an FBG to a diaphragm may have presented opportunities for inconsistencies that are difficult to evaluate and overcome given limitations of setting and precision of construction.

The novelty of this design lies in the incorporation of an FBG as the sensing element of the sensor which offers benefits relative to alternative sensing methods. These benefits include the small size an FBG sensor is contained in, the passive components operate for long lifetimes, fibre optic cables operate with little losses which allows transmission of signals over tens of kilometres, the lack of electrical signals renders FBGs suitable for challenging environments with explosion hazards, FBGs do not experience interference in the presence of electromagnetic radiation. However, for deep ocean applications, the primarily benefit of an FBG-based design is that it enables many sensors, installed on a single optical fibre, to be monitored by a single interrogation unit based on wavelength multiplexing. In summary, despite the inconsistencies observed between experimental configurations, a working configuration was developed that honored the design specifications.

Chapter 6 - Conclusions

6.0 Introduction

The necessity to understand phenomena that transpire in the open ocean provides motivation in designing ocean-bottom pressure sensors. These sensors can be applied to probe into the occurrences of vertical seafloor deformation or in the detection of tsunami. In doing so, an understanding of underlying principles of these phenomena can be gathered and be utilized for hazard prevention and warning systems.

A significant challenge with developing ocean-bottom sensors stems from the large contrast between the target pressure resolution and the ambient operating hydrostatic pressures experienced by these types of sensors. The sensor design studied in this thesis intends to resolve 1 cmH_2O within at a target depth of 2500 mH_2O. Given this difference in magnitudes, a sensor must adopt a form of pressure compensation to identify tsunami or ongoing vertical seafloor deformation. Developing a compatible pressure compensation technique forms one of the primary research objectives for this thesis.

A design that attempts to address this challenge with an FBG-diaphragm transducer is proposed. A dual chamber configuration in the sensor housing with a pressure-equilibrating piston provides pressure compensation by allowing both the face of the diaphragm externally exposed to seawater and internal face to experience the same hydrostatic pressure. The piston translates, changing the internal volume of the chamber when an external change in pressure occur and, thus, equilibrates the internal chamber to the external pressure. Based on this principle, a set of fundamental expressions are defined to develop a theoretical model for the formation of a series of design curves; used to form an understanding how each design parameter changes sensitivity. The practical aspect of this thesis is explored through experiments of two sensor builds that resemble but do not entirely embody the design concept.

An FEA is also performed to determine if the presence of an FBG would significantly reinforce the diaphragm. The results of the analysis indicate a loss of under 5% in strain with a bonded FBG.

The experimental evaluation of the sensor design for atmospheric testing produced a response performance that adhered to theory when the initial measurements were disregarded. The experimental examination of the differential pressure sensor design was observed to have similar characteristics. All of the experimental sensitivities beyond the prestressed states demonstrated strong linearity and the mean sensitivities at each target depth pressure were no different than 6% with respect to the theoretical model.

The largest challenge in this work was in obtaining consistency with different diaphragm samples and FBG bonds. This likely due to the bonding process of the FBG with the diaphragm, from applying and curing of the adhesive. A total of 12 samples were constructed and a quarter of these functioned as intended. To manufacture samples in quantity, multiple sheets of shim stock can be lathed using the described method in Section 4.1.2.

In summary, this work demonstrates that the sensor response to hydrostatic pressure changes achieved the sensitivity requirements set out in Figure 19. The FEA was able to rule out any significant concerns due to geometric and material similarities such as a possible reinforcing effect from an FBG. The linearity of the sensor was observed to occur beyond a certain threshold of pressure which is likely due to a combination of error associated with bonding and the diaphragm fixture method. It is of utmost importance that fabrication of the transducer produces a consistently functional output if the design is to be continued in future projects. The testing conducted in Section 5.3.1 which examined the relationship between the high-side and low-side pressure of differential transducer indicated the housing configuration has potential to operate successfully and consistently for the continued work.

6.1 Future work and technical risks

Despite laying some of the groundwork for a potential ocean-bottom pressure sensor, the subsequent steps required to develop a fully ocean-deployable sensor are considerable. There are several technical risks that should be observed, as they can raise concerns about the future viability of this venture. As mentioned previously, developing a consistently functioning FBG-diaphragm transducer is essential to future progression and the lack of this observed as the greatest risk associated during the course of this work. This is essential to ensuring that a final design operates reliably and over a long lifetime. If improving upon the bonding procedure or finding a proven method of adhering the FBG results in a consistently reliable outcome, the project would proceed by fabricating the final design concept (Figure 11) and testing in a controlled lab setting and ultimately the ocean.

Secondary risks arise from the development of the final sensor design, which includes the sliding piston head, the reliability of the check valves, and the diaphragm support plug. With regards to the piston, in principle it would consent no differential pressure between the two surfaces of the diaphragm when the sensor is descending during deployment however a further examination is required to determine whether this holds true in practice.

If the pressure needed to overcome the static friction of the piston is greater than what can be safely deflected by the diaphragm without damage, the mechanism will not be viable. Furthermore, the presence of some dynamic friction may cause some inherent deflection to be present in the diaphragm even after the sensor reaches its resting position, decreasing the overall operating range of the sensor.

The use of check valves provides a simple method of allowing water to enter the sensor housing while providing a failsafe for the diaphragm in the occurrence of sudden and immense pressure surges. The cracking pressure of the check valves would have to be finely tuned to allow the sensor to operate within the linear pressure range of the diaphragm. In addition, their use should not function with major latency and would have to operate in harmony with the piston.

The plug that supports the diaphragm before and during its deployment is another consideration for future work. If the diaphragm is to be supported in this manner, the plug has to allow the diaphragm to still experience exposure to water, be it through a small cut-out, a porous material, or some other technique. The secondary regard is the disengagement method of the plug when the resting position is reached. This could be facilitated by constructing the plug out of a dissolvable material or the use of corroding links that cause the parts to separate.

A tertiary risk is associated with the eventual introduction to ocean testing and ultimately full-scale deployment. Given the unforgiving and uncontrollable nature of the ocean, the sensor itself has to have a rugged structure along with the adequate mooring cables that feed to the buoy. Fibre optic mooring cables would be under a considerable amount of tensile stress and thus the proper material and design must be put in place. Mooring cables can be fabricated out of nylon, polyester, and Vectran and have been tested to deployment depths of up to 5000m in some past literary works [35]. Overcoming these hurdles and developing this sensor successfully would be an important step towards creating potential interest in the oceanographic monitoring industry.

References

[1] k. Suzuki, E. Araki and N. Takahashi, "Detectability of crustal deformation by using ocean bottom pressure gauges deployed to DONET system," in *OCEANS - MTS/IEEE Kobe Techno-Oceans Conference*, Kobe, 2018.

[2] T. Muramoto, Y. Ito, D. Inazu, L. M. Wallace, R. Hino and S. Suzuki, "Seafloor crustal deformation on ocean bottom pressure records with nontidal variability corrections: Application to Hikurangi margin, New Zealand," *Geophysical Research Letters,* vol. 46, pp. 303-310, 2019.

[3] W. W. Chadwick Jr, S. L. Nooner, M. A. Zumberge, R. W. Embley and C. G. Fox, "Vertical deformation monitoring at Axial Seamount since its 1998 eruption using deep-sea pressure sensors," *Journal of Volcanology and Geothermal Research,* vol. 150, pp. 313-327, 2006.

[4] Australian Government, "Tsunami," Geoscience Australia, [Online]. Available: https://www.ga.gov.au/scientific-topics/community-safety/tsunami. [Accessed 03 December 2019].

[5] International Tsunami Information Center, "How does tsunami energy travel across the ocean and how far can tsunamis waves reach?," UNESCO, 2019. [Online]. Available: http://itic.ioc-unesco.org/index.php?option=com_content&view=article&id=1164:how-does-tsunami-energy-travel-across-the-ocean-and-how-far-can-tsunamis-waves-reach&catid=1340&Itemid=2031.

[6] C. E. Synolakis, "Green's law and the evolution of solitary waves," *Phys. Fluids A,* vol. 3, no. 3, pp. 490-491, 1991.

[7] G. Margaritondo, "Explaining the physics of tsunamis to undergraduate and non-physics students," *European Journal of Physics,* vol. 26, pp. 401-407, 2005.

[8] A. B. Rabinovich, "Tsunami observations in the open ocean," *Izvestiya, Atmospheric and Oceanic Physics,* vol. 50, no. 5, pp. 445-458, 2014.

[9] Department Of The Navy, "Navy Supplement to the DOD Dictionary of Military and Associated Terms," August 2006. [Online]. Available: https://www.nwdc.navy.mil/Documents/NTRP_1-02.pdf. [Accessed January 2020].

[10] E. N. Bernard and C. Meinig, "History and Future of Deep-Ocean Tsunami," in *OCEANS'11 MTS/IEEE KONA*, Waikoloa, USA, 2011.

[11] Sea-Bird Scientific, "SBE 50 Digital Oceanographic Pressure Sensor," October 2018. [Online]. Available: https://www.seabird.com/asset-get.download.jsa?id=54627862104. [Accessed 15 November 2018].

[12] Valeport, "miniIPS - Intelligent Pressure Sensor," July 2016. [Online]. Available: http://www.valeport.co.uk/Portals/0/Docs/Datasheets/Valeport-miniIPS.pdf. [Accessed 17 November 2018].

[13] General Electric, "The PRECISE DPS2000 Series Digital Pressure Transmitter," September 2016. [Online]. Available: https://www.industrial.ai/sites/g/files/cozyhq596/files/2018-07/920-667a.pdf. [Accessed 17 November 2018].

[14] Paroscientific Inc., "Submersible Depth Sensors Series 8000," May 2015. [Online]. Available: https://www.innova.no/wp-content/uploads/2015/05/Paroscientifc_Digiquartz_heads.pdf. [Accessed 20 November 2018].

[15] P. Regtien and E. Dertien, "Resistive Sensors," in *Sensors for Mechatronics*, Amsterdam, Elsevier, 2019, pp. 57-101.

[16] NOAA, "Bottom Pressure Recorder," Deep-ocean Assessment and Reporting of Tsunamis, [Online]. Available: https://nctr.pmel.noaa.gov/Dart/gauge.html. [Accessed 5 December 2019].

[17] C. Meinig, S. E. Stalin and A. I. Nakamura, *Real-Time Deep-Ocean Tsunami Measuring, Monitoring, and Reporting System: The NOAA DART II Description and Disclosure,* NOAA, Pacific Marine Environmental Laboratory (PMEL), 2005.

[18] P. V. Rao, K. Srimannarayana, M. S. Shankar and P. Kishore, "Diaphragm based high sensitive FBG pressure sensor," in *International Conference on Optics in Precision Engineering and*, Singapore, 2013.

[19] J. Huang, Z. Zhou, X. Wenb and D. Zhang, "A diaphragm-type fiber Bragg grating pressure sensor with temperature compensation," *Measurement,* vol. 43, pp. 1041-1046, 46.

[20] G. Allwood, G. Wild, A. Lubansky and S. Hinckley, "A highly sensitive fiber Bragg grating diaphragm pressure transducer," *Optical Fiber Technology,* vol. 25, pp. 25-32, 2015.

[21] C. Marques, G.-D. Peng and D. J. Webb, "Highly sensitive liquid level monitoring system utilizing polymer fiber Bragg gratings," *Optics Express,* vol. 23, no. 5, pp. 6058-6072, 2015.

[22] C. Díaz, A. Leal-Junior, P. André, P. Fernando da Costa Antunes, M. J. Pontes, A. Frizera-Neto and M. R. N. Ribeiro, "Liquid Level Measurement Based on FBG-Embedded Diaphragms with Temperature Compensation," *IEEE Sensors Journal,* vol. 18, no. 1, pp. 193-200, 2018.

[23] M.-f. Liang, X.-q. Fang, G. Wu, G.-z. Xue and H.-w. Li, "A fiber bragg grating pressure sensor with temperature compensation based on diaphragm-cantilever structure," *Optik,* vol. 145, p. 503–512, 2017.

[24] W. Zhang, F. Li, Y. Liu and H. Xiao, "FBG Hydrophone: Theory and Experiment," in *2008 1st Asia-Pacific Optical Fiber Sensors Conference*, Chengdu, 2008.

[25] U. K. Chandrika, V. Pallayil, K. M. Lim and C. H. Chew, "Pressure compensated fiber laser hydrophone: Modeling and experimentation," *The Journal of the Acoustical Society of America,* vol. 134, p. 2710–2718, 2013.

[26] H.-H. Gennerich and H. Villinger, "A new concept for an ocean bottom pressure meter capable of precision long-term monitoring in marine geodesy and oceanography," *Earth,* vol. 2, pp. 181-186, 2015.

[27] J. Wei, "Multiplexed FBG sensors and their applications," in *International Symposium on Photonics and Applications*, Singapore, 1999.

[28] Water Properties Group, "Science Guidelines," Water Properties Group, [Online]. Available:

https://www.waterproperties.ca/mainlogin.php?refer=/public/scienceguidelines.php. [Accessed 9 April 2020].

[29] Vishay Preciscion Group, "Design Considerations for Diaphragm Pressure Transducers," 1 November 2010. [Online]. Available: http://www.vishaypg.com/doc?11060. [Accessed 27 December 2018].

[30] W. C. Young and R. G. Budynas, Roark's Formulas for Stress and Strain, New York: McGraw-Hill, 2002.

[31] W. P. Eaton, F. Bitsie, J. H. Smith and D. W. Plummer, "A new analytical solution for diaphragm deflection and its application to a surface-micromachined pressure sensor," in *International Conference on Modeling and Simulation of Microsystems*, San Juan, 1999.

[32] Sakurambo, "A Fiber Bragg Grating structure, with refractive index profile and spectral response," 2 July 2008. [Online]. Available: https://en.wikipedia.org/w/index.php?curid=18248811. [Accessed 27 November 2019].

[33] D. Sengupta, "Fiber Bragg Grating Sensors and Interrogation Systems," in *Optical Fiber Sensors Advanced Techniques and Applications*, Boca Raton, Taylor & Francis Group, 2015, pp. 207-256.

[34] M. J. Moran, H. N. Shapiro, D. D. Boettner and M. B. Bailey, Fundamentals of Engineering Thermodynamics, Hoboken: John Wiley & Sons, Inc., 2014.

[35] M. A. Grosenbaugh, W. Paul, D. Frye and N. Farr, "Development of Synthetic Fiber-Reinforced Electro-Optical-Mechanical Cables for Use With Moored Buoy Observatories," *IEEE JOURNAL OF OCEANIC ENGINEERING,* vol. 31, no. 3, pp. 574-585, 2006.

[36] S. K. Jindal and S. K. Raghuwanshi, "A complete analytical model for circular diaphragm pressure sensor with freely supported edge," *Microsystem Technologies,* vol. 21, no. 5, pp. 1073-1079, 2015.

[37] A. B. Rabinovich and M. C. Eblé, "Deep-Ocean Measurements of Tsunami Waves," *Pure and Applied Geophysics,* vol. 172, no. 12, pp. 3281-3312, 2015.

[38] D. Pugh and P. Woodworth, Sea-Level Science: Understanding Tides, Surges, Tsunamis and Mean Sea-Level Changes, Cambridge: Cambridge University Press, 2014.

[39] A. Rabinovich, Long Ocean Gravity Waves: Trapping, Resonance, and Leaking, Leningrad: Gidrometeoizdat, 1993, p. 325.

[40] Sea-Bird Scientific, "About Sea-Bird Scientific," Sea-Bird Scientific, 2018. [Online]. Available: https://www.seabird.com/about-sea-bird. [Accessed 15 November 2018].

[41] É. Pinet, "Pressure measurement with fiber-optic sensors: Commercial technologies and applications," in *21st International Conference on Optical Fibre Sensors*, Ottawa, 2011.

[42] R. B. Northrop, Introduction to Instrumentation and Measurements, Boca Raton: Taykir & Francis Group, 2005.

[43] D. M. Stefanescu, Handbook of Force Transducers, Berlin: Springer, 2011.

[44] R. Kashyap, Fiber Bragg Gratings, Montreal: Elsevier Inc, 2009.

[45] R. M. Measures, Structural Monitoring with Fiber Optic Technology, London: Academic Press, 2001.

[46] G. A. Ramadass, N. Vedachalam, T. Sudhakar, R. Ramesh, V. B. N. Jyothi, N. B. Prashanth and M. A. Atmanand, "A Study of the Algorithms for the Detection of Tsunami Using an Ocean Bottom Pressure Recorder," *Marine Technology Society Journal,* vol. 48, no. 1, pp. 76-83, 2014.

[47] M. G. Xu, L. Reekie, U. T. Chow and J. P. Dakin, "Optical in-fiber grating high pressure sensor," *Electronics Letters ,* vol. 29, no. 4, pp. 398-399, 1993.

[48] V. Pachava, S. Kamineni, S. Madhuvarasu and K. Putha, "A high sensitive FBG pressure sensor using thin metal diaphragm," *Journal of Optics,* vol. 43, no. 2, pp. 117-121, 2014.

Appendix A - Theoretical Model Scripts

$$\frac{d\lambda}{d\Delta P_{ext}} = 1.209a^2\,(v^2\; - \;1)10^8\left(3\left(\frac{A}{B} + \frac{v^2 - 1}{16(v\; - \;1)(v\; + \;1)Et^2}\right) - \frac{3}{8Et^2}\right) \qquad (6.1)$$

Where:

$$A = a^8(P_{ext} +\; \Delta P_{ext}) -\; 2a^8v^2(P_{ext} + \Delta P_{ext}) +\; a^8v^4(P_{ext} +\; \Delta P_{ext}) +\; 16Ea^4 l_f t^3(v^2 - 1)$$

$$B = 16a^4(v\; - \;1)(v\; + \;1)Et^2\sqrt{C}$$

$$C = \left(a^8(P_{ext}^2 +\; \Delta P_{ext}^2 +\; 2P_{ext}\Delta P_{ext}) +\; 256E^2 l_f^2 t^6 - a^8v^2(2P_{ext}^2 - 2\Delta P_{ext}^2 -\; 4P_{ext}\Delta P_{ext}) + a^8v^4(P_{ext}^2 +\; \Delta P_{ext}^2 + 2P_{ext}\Delta P_{ext}) +\; 32Ea^4 l_f t^3(P_{ext} - \Delta P_{ext}) +\; 32Ea^4\, l_f t^3 v^2(\Delta\, P_{ext} - P_{ext})\right)$$

The following analysis are unique and were developed by the author.

Script 1

```
% Theoretic Sensor Model Sensitivity vs Diaphragm Thickness Output
% This script computes sensitivity for the sensor model described Section 3.2
and develops a plot of sensitivity across varying diaphragm geometric
properties


%Diaphragm Parameters
E= 193*10^9;%1.93e11; % Young's Modulus (Pa)
v= 0.265; % Poisson's Ratio

for (i=1:1:300)   %computes sensitivity vs diaphragm geometry
t= 0.0001+0.000001*i; % diaphragm thickness (m)
th(i)=t*1000;
a=0.005:0.005:0.03;% diaphragm radius (m)

Patm=101325; %Atmospheric Pressure (Pa)
li=15; %Initial Length of Chamber A (cm)
Pdepm=500; %Target depth (m)
Pdep=Pdepm*9.81*1000; %Pressure due to depth (Pa)
Ppre=Pdep*0.750; %Pressure preload (Pa)
Pf= Pdep+Patm; % Final Pressure at depth(Pa)
lf=((Patm+Ppre)/Pf)*li; %Final Length of Chamber A (m)

As=pi*((a*100).^2); % Circular Area of Sensor (cm2)
Vi=As*li; %Initial Volume in Sensor Chamber A (cm3)
```

```
Vf=As*lf; %Final Volume in Sensor Chamber A (cm3)

g=9.81; %gravity (m/s2)
rho=1000; %density of water (kg/m3)
Papp= 0.01*g*rho; % ΔPext, Change in pressure from 1 cm head(Pa)

proots=[1 Pf-Papp+((16*E*lf*(t^3))./((a.^4)*(1-(v^2)))) -(Pf*Papp)]; % Equation
(3.11)
Pint= roots(proots);
Pint=Pint(2);

y(:,i)=(3*(Papp-Pint)*(a.^4)*(1-(v^2)))/(16*E*(t^3)); % Center deflection (m)

deltaVa(:,i)=(pi*(Papp-Pint).*(a.^6)*(1-(v^2)))/(16*E*(t^3)); % Volume change
due to deflection, % ΔVa(m3)

%Output
deltastrain(:,i)=-(a.^2.*(v.^2 - 1).*((3.*(a.^4 + (2.*Papp.*a.^8 + 2.*Pf.*a.^8
- 4.*Papp.*a.^8.*v.^2 + 2.*Papp.*a.^8.*v.^4 - 4.*Pf.*a.^8.*v.^2 +
2.*Pf.*a.^8.*v.^4 - 32.*E.*a.^4.*lf.*t.^3 +
32.*E.*a.^4.*lf.*t.^3.*v.^2)./(2.*(Papp.^2.*a.^8 + Pf.^2.*a.^8 +
256.*E.^2.*lf.^2.*t.^6 - 2.*Papp.^2.*a.^8.*v.^2 + Papp.^2.*a.^8.*v.^4 -
2.*Pf.^2.*a.^8.*v.^2 + Pf.^2.*a.^8.*v.^4 + 2.*Papp.*Pf.*a.^8 -
4.*Papp.*Pf.*a.^8.*v.^2 + 2.*Papp.*Pf.*a.^8.*v.^4 - 32.*E.*Papp.*a.^4.*lf.*t.^3
+ 32.*E.*Pf.*a.^4.*lf.*t.^3 + 32.*E.*Papp.*a.^4.*lf.*t.^3.*v.^2 -
32.*E.*Pf.*a.^4.*lf.*t.^3.*v.^2).^(1./2)) - a.^4.*v.^2))./(2.*a.^4.*(v - 1).*(v
+ 1)) + 3))./(8.*E.*t.^2); %change in microstrain in diaphragm {expanded
version of Equation 3.16)

sens=(deltastrain*1.209*Papp*10^6); %sensitivity computation (from 0 -> Papp)

lin(:,i)=(16*E*(t^4))./(3*(a.^4)*(1-(v^2))); % pressure limit for linearity
(Pa)
end

plot(th,sens)
xlabel('Diaphragm Thickness (mm)','fontsize',30)
ylabel('Sensitivity (pm/cmH_2O)','fontsize',30)
hleg=legend('10 mm','20 mm','30 mm','40 mm','50 mm','60 mm');
htitle = get(hleg,'Title');
set(gca,'FontSize',30);
set(htitle,'String','Diaphragm Diameter');
set(groot,'defaultLineLineWidth',3.0);
grid(gca,'minor')
```

Script 2

```
% Theoretic Sensor Model Sensitivity vs Preload Output
%This script computes sensitivity for the sensor model described Section 3.2
and develops a plot of sensitivity across varying sensor lengths and pressure
preloads
```

```
%Diaphragm Parameters
E= 193*10^9;% Young's Modulus (Pa)
v= 0.265; % Poisson's Ratio
t=0.0001; % Diaphragm thickness (m)
a=0.0255;% Diaphragm radius (m)

for (i=1:1:101)

Pdepm=2500; %Target Depth (m)
Pdep=Pdepm*9.81*1000; %Pressure due to depth (Pa)
Ppre=Pdep*((0.01*i)-0.01); %Pressure Preload (Pa)

Patm=101325; %Atmospheric Pressure (Pa)
li=5:5:25; %Initial Lengths of Chamber A (cm)

Pf= Pdep+Patm; %Final Pressure at depth (Pa)
lf=((Patm+Ppre).*(li))./Pf; %Final Length of Chamber A (m)

As=pi*((a*100)^2); % Circular Area of Sensor (cm2)
Vi=As*li; %Initial Volume in Sensor Chamber A (cm3)
Vf=As*lf; %Final Volume in Sensor Chamber A (cm3)

g=9.81; %gravity (m/s2)
rho=1000; %density of water (kg/m3)
Papp= 0.01*g*rho; % ΔPext, Change in pressure from 1 cm head(Pa)

proots=[1 Pf-Papp+((16*E*lf*(t^3))./((a.^4)*(1-(v^2)))) -(Pf*Papp)]; % Equation
(3.11)
Pint= roots(proots);
Pint=Pint(2);

y(:,i)=(3*(Papp-Pint)*(a.^4)*(1-(v^2)))/(16*E*(t^3)); % Center deflection (m)

deltaVa(:,i)=(pi*(Papp-Pint).*(a.^6)*(1-(v^2)))/(16*E*(t^3)); % Volume change
due to deflection, % ΔVa(m3)

%Output
deltastrain(:,i)=-(a.^2.*(v.^2 - 1).*((3.*(a.^4 + (2.*Papp.*a.^8 + 2.*Pf.*a.^8
- 4.*Papp.*a.^8.*v.^2 + 2.*Papp.*a.^8.*v.^4 - 4.*Pf.*a.^8.*v.^2 +
2.*Pf.*a.^8.*v.^4 - 32.*E.*a.^4.*lf.*t.^3 +
32.*E.*a.^4.*lf.*t.^3.*v.^2)./(2.*(Papp.^2.*a.^8 + Pf.^2.*a.^8 +
256.*E.^2.*lf.^2.*t.^6 - 2.*Papp.^2.*a.^8.*v.^2 + Papp.^2.*a.^8.*v.^4 -
2.*Pf.^2.*a.^8.*v.^2 + Pf.^2.*a.^8.*v.^4 + 2.*Papp.*Pf.*a.^8 -
4.*Papp.*Pf.*a.^8.*v.^2 + 2.*Papp.*Pf.*a.^8.*v.^4 - 32.*E.*Papp.*a.^4.*lf.*t.^3
+ 32.*E.*Pf.*a.^4.*lf.*t.^3 + 32.*E.*Papp.*a.^4.*lf.*t.^3.*v.^2 -
32.*E.*Pf.*a.^4.*lf.*t.^3.*v.^2).^(1./2)) - a.^4.*v.^2))./(2.*a.^4.*(v - 1).*(v
+ 1)) + 3))./(8.*E.*t.^2); %change in microstrain in diaphragm {expanded
version of Equation 3.16)

sens=(deltastrain*1.209*Papp*10^6); %sensitivity computation (from 0 -> Papp)
```

```
lin(:,i)=(16*E*(t^4))./(3*(a.^4)*(1-(v^2))); % pressure limit for linearity (Pa)

Pprei(i)=(Ppre/Pdep); %For plotting preload vs sensitivity

end
plot(Pprei,sens)
xlabel('Preload Factor (%)','fontsize',20)
ylabel('Sensitivity (pm/cm H2O)','fontsize',20)
hleg=legend('50 mm','100 mm','150 mm','200 mm','250 mm');
htitle = get(hleg,'Title');
set(gca,'FontSize',25);
set(htitle,'String','Sensor Length (l_i)');
set(groot,'defaultLineLineWidth',3.0);
grid(gca,'minor')
```

Script 3

```
% Theoretic Sensor Model Sensitivity vs Depth Output
%This script computes sensitivity for the sensor model described Section 3.2 and develops a plot of sensitivity across Depths and Preloads

%Diaphragm Parameters
E= 193*10^9;% Young's Modulus (Pa)
v= 0.265; % Poisson's Ratio
t=0.0001; % Diaphragm thickness (m)
a=0.0255;% Diaphragm radius (m)

g=9.81; %gravity (m/s2)
rho=1000; %density of water (kg/m3)
Papp= 0.01*g*rho; % ΔPext, Change in pressure from 1 cm head(Pa)

%Sensor Housing and Calcs
Patm=101325; %Atmospheric Pressure (Pa)
li=3; %Initial Length of Chamber A (cm)

for (i=1:1:2500)
Pdep= i*rho*g; %Pressure due to depth (Pa)
Ppre=Pdep*[0:0.20:1]; %Pressure preload (Pa)
Pf= Pdep+Patm; %Final Pressure at depth (Pa)
lf=((Patm+Ppre)/Pf)*li; %Final Length of Chamber A (m)

As=pi*((a*100)^2); % Circular Area of Sensor (cm2)
Vi=As*li; %Initial Volume in Sensor Chamber A (cm3)
Vf=As*lf; %Final Volume in Sensor Chamber A (cm3)

proots=[1 Pf-Papp+((16*E*lf*(t^3))./((a.^4)*(1-(v^2)))) -(Pf*Papp)]; % Equation (3.11)
Pint= roots(proots);
Pint=Pint(2);
```

```
y(:,i)=(3*(Papp-Pint)*(a.^4)*(1-(v^2)))/(16*E*(t^3)); % Center deflection (m)

deltaVa(:,i)=(pi*(Papp-Pint).*(a.^6)*(1-(v^2)))/(16*E*(t^3)); % Volume change
due to deflection, % ΔVa(m3)

%Output
deltastrain(:,i)=-(a.^2.*(v.^2 - 1).*((3.*(a.^4 + (2.*Papp.*a.^8 + 2.*Pf.*a.^8
- 4.*Papp.*a.^8.*v.^2 + 2.*Papp.*a.^8.*v.^4 - 4.*Pf.*a.^8.*v.^2 +
2.*Pf.*a.^8.*v.^4 - 32.*E.*a.^4.*lf.*t.^3 +
32.*E.*a.^4.*lf.*t.^3.*v.^2)./(2.*(Papp.^2.*a.^8 + Pf.^2.*a.^8 +
256.*E.^2.*lf.^2.*t.^6 - 2.*Papp.^2.*a.^8.*v.^2 + Papp.^2.*a.^8.*v.^4 -
2.*Pf.^2.*a.^8.*v.^2 + Pf.^2.*a.^8.*v.^4 + 2.*Papp.*Pf.*a.^8 -
4.*Papp.*Pf.*a.^8.*v.^2 + 2.*Papp.*Pf.*a.^8.*v.^4 - 32.*E.*Papp.*a.^4.*lf.*t.^3
+ 32.*E.*Pf.*a.^4.*lf.*t.^3 + 32.*E.*Papp.*a.^4.*lf.*t.^3.*v.^2 -
32.*E.*Pf.*a.^4.*lf.*t.^3.*v.^2).^(1./2)) - a.^4.*v.^2))./(2.*a.^4.*(v - 1).*(v
+ 1)) + 3))./(8.*E.*t.^2); %change in microstrain in diaphragm {expanded
version of Equation 3.16)

sens=(deltastrain*1.209*Papp*10^6); %sensitivity computation (from 0 -> Papp)

lin(:,i)=(16*E*(t^4))./(3*(a.^4)*(1-(v^2))); % pressure limit for linearity
(Pa)

Pdepm(i)=Pdep/(rho*g); %For plotting sensitivity vs depth

end


plot(Pdepm,sens)
xlabel('Target Depth (mH20)','fontsize',16)
ylabel('Sensitivity (pm/cm H2O)','fontsize',16)

hleg=legend('0%','20%','40%','60%','80%','100%');
htitle = get(hleg,'Title');
set(gca,'FontSize',25);
set(htitle,'String','Preload Factor (k)');
set(groot,'defaultLineLineWidth',3.0);
grid(gca,'minor')
```

Appendix B - Experimental Equipment and Full Diaphragm Properties

The following fundamental hardware is used to carry out the experiments for Section 4.2.1:

- Screw pump (High Pressure Generator #87-6-5, High Pressure Equipment Co, Erie, PA)
- Differential pressure transducer (Omega© PX409-005DDU5V, 0-5psid, ±0.05%FSO, Omega Engineering Inc., Stamford, CT)
- Optical wavelength interrogator (sm130 Optical Sensing Interrogator, Micron Optics Inc, Atlanta, GA)
- Push-to-connect valve (McMaster Carr, Elmhurst, IL)
- Various types of push-to-connect fittings (McMaster Carr, Elmhurst, IL)
- ¼” Nylon tubing (McMaster Carr, Elmhurst, IL)

The following fundamental hardware is used to carry out the experiments for Section 4.2.2:

- Screw pump (High Pressure Generator #87-6-5, High Pressure Equipment Co, Erie, PA)
- Differential pressure transducer (Omega© PX409-005DDU5V, 0-5psid, ±0.05%FSO, Omega Engineering Inc., Stamford, CT)
- Single-sided pressure transducer (Omega© PX409-100G10V-EH, 0-100psig, ±0.05%FSO, Omega Engineering Inc., Stamford, CT)
- Optical wavelength interrogator (sm130 Optical Sensing Interrogator, Micron Optics Inc, Atlanta, GA)

- Air tank (Viair 91014 1 Gallon, VIAIR CORP, Irvine, CA)
- Pressure Regulator (PRS301243, Prostar, Praxair, INC, Danbury, CT)
- Swagelok Poppet Check Valve, Adjustable Pressure, 50 to 150 psig (x2) (SS-4CPA4-50, Swagelok Co, Solon, OH)
- Push-to-connect valves (x2) (McMaster Carr Co, Elmhurst, IL)
- Various types of push-to-connect fittings (McMaster Carr Co, Elmhurst, IL)
- ¼” Nylon tubing (McMaster Carr Co, Elmhurst, IL)

Table 8: Sensor Design Parameters

	Parameter	**Specification**
Diaphragm	Radius (mm)	25.05
	Thickness (mm)	0.1524
	Material Type	316 Stainless Steel
	Young's Modulus (GPa)	193
	Poisson Ratio	0.27
	Linearity Range (Pa)	705.9
	Linearity Range (cmH_2O)	7.2
Single-Mode Fibre	Diameter (µm)	203
	Length (mm)	6
	Young's Modulus (GPa)	67
	Poisson Ratio	0.27
	FBG Length (mm)	3
	Centre Wavelength (nm)	1550 +/-1
	FWHM (nm)	0.65 +/-0.2
	Reflectivity (%)	>50
	Fibre Type	SMF-28C
	Fibre Recoating	None
Diaphragm Housing Structure	Inner Diameter (mm)	50.1
	Outer Diameter (mm)	61.52
	Sensor Length (mm)	60
	Preload Factor	0
	Material Type	Aluminum